Thermal characterization for quantum materials

Shucheng Guo,[1, a)] Youming Xu,[1, a)] Thomas Hoke,[1] Gobind Sohi,[1] Shuchen Li,[1] and Xi Chen[1, b)]

[1]Department of Electrical and Computer Engineering, University of California, Riverside, CA 92521, USA

[a)] Shucheng Guo and Youming Xu contributed equally to this work.

[b)] Author to whom correspondence should be addressed: xichen@ucr.edu.

ABSTRACT

Recently, the study of quantum materials through thermal characterization methods has attracted increasing attention. These methods, although not as widely used as electrical methods, can reveal intriguing physical properties in materials that are not detectable by electrical methods, particularly in electrical insulators. A fundamental understanding of these physical properties is critical for the development of novel applications for energy conversion and storage, quantum sensing and quantum information processing. In this review, we introduce several commonly used thermal characterization methods for quantum materials, including specific heat, thermal conductivity, thermal Hall effect and Nernst effect measurements. Important theories for the thermal properties of quantum materials are discussed. Moreover, we introduce recent research progress on thermal measurements of quantum materials. We highlight experimental studies on probing the existence of quantum spin liquids, Berry curvature, chiral anomaly and coupling between heat carriers. We also discuss the work on investigating the quantum phase transitions and quasi-particle hydrodynamics using thermal characterization methods. These findings have significantly advanced knowledge regarding novel physical properties in quantum materials. In addition, we provide some perspectives on further investigation of novel thermal properties in quantum materials.

Keywords: quantum materials; thermal conductivity; thermal Hall effect; specific heat; Nernst effect

I. INTRODUCTION

Quantum materials exhibit exotic physical properties, which arise from the quantum mechanical properties of their constituent particles or quasi-particles.[1] They are a class of materials whose quantum properties usually stem from the close relationship between dimensionality reduction, quantum confinement, quantum coherence, quantum fluctuations, topology of wavefunctions, relativistic spin–orbit interactions, fundamental symmetries and so on.[2] For instance, superconductivity is usually attributed to strong electronic correlations.[3–7] The novel electronic properties of topological insulators (TIs) are related to non-universal quantum effects.[8–10] Moreover, topological Dirac and Weyl semimetals,[11–16] quantum spin liquids (QSLs),[17–19] spin superfluidity,[20] graphene, low-dimensional van der Waals heterostructures[21–27] and Moiré materials[28] also belong to the general class of quantum materials that have been investigated extensively in recent years.

Lately, quantum materials have attracted increasing interest due to their widespread application in various fields and have such become a new cornerstone of basic science. Quantum materials

exhibit excellent energetic properties in terms of energy transmission, conversion, and storage. Superconductors are particularly useful in energy transmission, as they can be applied in long-distance and low-voltage electric grids without any transmission loss.[29] Two-dimensional (2D) materials such as graphene and boron nitride excel in energy conversion and storage with applications in catalysis, fuel cells, batteries, and photovoltaics. [30,31] Furthermore, owing to the quantum Hall effect (QHE) and the anomalous Hall effect (AHE),[32] TIs are good candidates for spintronic and optoelectronic devices.[33,34] Dirac and Weyl semimetals are three-dimensional (3D) phases of matter with gapless electronic excitations,[35] which can be used in topological quantum computation and to build fault-tolerant quantum computers.[36,37] TIs, and Dirac and Weyl semimetals, which are characterized by their nontrivial electronic topology, also prove to be promising thermoelectric materials for waste heat recovery.[38] In the emerging fields of quantum computing and quantum information storage, utilizing the non-trivial excitations of QSLs could greatly improve the existing computing technology.[39] Moreover, superconductive 2D materials are promising solid-state platforms for quantum dot qubits, single-photon emitters, superconducting qubits and topological quantum computing elements.[39,40] In biomedical applications, quantum dots can be used as fluorophores for imaging and detection purposes in cell targeting, delivery, diagnosis, and cancer treatment research.[41–43]

In order to develop advanced material applications for quantum materials, accurately characterizing their quantum properties is paramount. Due to the low temperature (T) requirement and subsequent suppressed thermal fluctuations of many quantum effects such as the QHE, electrical measurements are typically employed to investigate quantum materials.[44] Common thermal property measurements used for the characterization of quantum materials include specific heat (C), thermal conductivity (κ), and thermal Hall conductivity (κ_{xy}) measurements. Additionally, the Nernst effect, which combines electrical and thermal measurements, is also an important tool for studying novel topological properties. Thermal property measurements can provide critical information that cannot be obtained from electrical measurements, especially in the case of some electrical insulators, such as TIs and QSLs. Compared with electrical measurement methods, thermal transport measurements have the distinct advantage of detecting charge-neutral excitations, such as lattice vibrations (phonons) and spin excitations. In insulators where conduction electrons are absent, thermal transport measurements provide exclusive access to the physical nature of charge-neutral heat carriers.[45] Furthermore, thermal characterization methods provide unique and important insight into the density, mobility and scattering of heat carriers at both marco- and nano-scales. These measurements can usually be carried out using standard laboratory equipment without relying on other sophisticated instruments and rare resources.

In crystalline materials, the total thermal conductivity (κ_{tot}) can be expressed as

$$\kappa_{tot} = \kappa_e + \kappa_{ph} + \kappa_{spin} + \kappa_{other},$$

where κ_e, κ_{ph} and κ_{spin} come from the contributions of electrons, phonons, and spin excitations respectively, and κ_{other} arises from other contributions. The mean free path (MFP) and transport mechanisms of heat carriers can be obtained by analyzing κ and its T dependence.[46] Such information can also be used to study quasi-particle hydrodynamics.[47,48] Furthermore, κ measurements are sensitive exclusively to entropy-carrying itinerant spin excitations, which can provide important information on the nature of spin correlation and coupling of spin with other heat carriers.[49–51] Spin excitations carry no charge and are therefore difficult to be measured by electrical methods. In particular, itinerant quasi-particles related to certain quantum states can significantly

contribute to thermal transport at low T. As such, ultralow-T κ measurements have been adopted to identify the emerging QSLs.[52,53] Aside from κ measurements, thermal Hall effect (THE) measurements shift the focus from longitudinal transport to transverse transport. THE measurements are not only useful for probing charge-neutral edge states, such as confirming the existence of nontrivial topology,[44] but also in characterizing uncharged edge states, such as the discovery of charge-neutral Majorana fermions in QSLs and topological superconductors.[54–56] The Nernst effect measurements, which can effectively detect topological band structures,[57] can be used to study topological/quantum phase transitions,[58,59] and spin excitations.[60] In addition, in some topological Weyl semimetals, anomalous Nernst effect (ANE) can be treated as a signature for Berry curvature near the Fermi level.[61] In turn, it can easily be seen that thermal property measurements are an important and unique tool for probing the emerging quantum materials.

Recently, an excellent review paper[44] by Li and Chen discussed the critical role of thermal transport in understanding quantum materials. They introduced three examples studying QSLs, superconductors, and topological Weyl semimetals using bulk thermal transport measurements. In addition to these measurements, our review also introduces several other important thermal characterization methods, such as specific heat and nanoscale thermal transport measurements. We also discuss new experimental findings after the publication of the review paper by Li and Chen. It should be noted that we do not cover the electron microscopy based thermal characterization techniques. Interested readers can consult the recent review papers.[62,63]

This review is organized as follows. In section II, we introduce the basic theories of thermal properties in quantum materials, including heat carriers in quantum materials, kinetic theory of thermal transport, and Berry curvature theory for the THE and ANE. Several thermal characterization methods are also briefly discussed. Section III highlights selected advances in exploring quantum materials through thermal property measurements. In the end, we provide some perspectives about the impact of thermal characterization on the future investigation of quantum materials in section IV.

II. BASIC THEORIES OF THERMAL PROPERTIES IN QUANTUM MATERIALS AND THERMAL CHARACTERIZATION METHODS

A. Heat carriers in quantum materials

In quantum materials, heat can be carried by various particles or quasi-particles, such as phonons, electrons, and spin excitations (Fig. 1). Spin excitations include magnons with spin $S = 1$, spinons with $S = 1/2$ and others. The basic properties of these heat carriers are summarized in Table 1. The thermal transport mechanisms of these quasi-particles are discussed below.

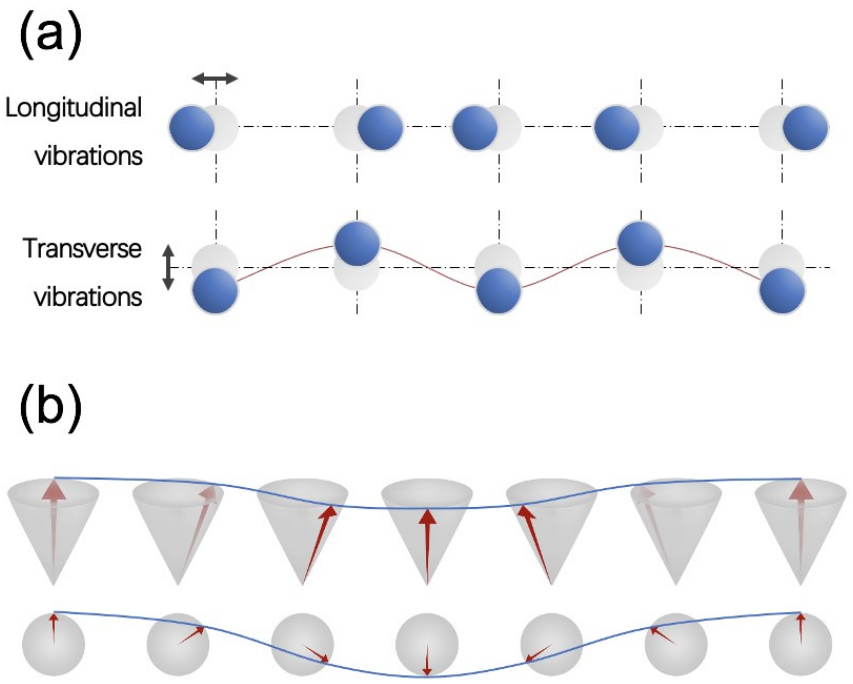

Figure. 1: *Schematic diagrams of (a) phonons and (b) spin excitations.*

Table 1. Heat carriers in quantum materials

Heat carrier	Essence	Type
Phonon	Lattice vibration	Boson
Electron	Charged subatomic particle	Fermion
Magnon	Collective spin excitation with spin-1	Boson
Spinon	Collective spin excitation with spin-1/2	Fermion

1. Phonon

Phonons are collective excitations in a periodic, elastic arrangement of atoms or molecules (Fig. 1a).[64,65] The concept of phonon was first introduced by Igor Tamm in 1932. At $T = 0$ K, there are no phonons as the crystal lattice is in the ground state. At finite T, the energy fluctuation caused by random lattice vibration can be regarded as a kind of phonon gas. Therefore, phonons are directly related to the thermodynamic properties of solids. The phonon contribution to specific heat in 3D systems is proportional to T^3 at low T according to the Debye model.[66] At high T, the specific heat approaches the Dulong-Petit limit of $3Nk_B$, where N is the number of atoms in the specimen, and k_B is the Boltzmann constant.[67] There are several types of phonon scattering mechanisms, including boundary scattering, Umklapp scattering, lattice imperfection scattering and electron-phonon scattering.[68]

Boundary scattering occurs when phonon MFP is of the same scale as the sample size.[69] Thermal boundary resistance is present at interfaces, and it is determined by the flux of heat carriers irradiating the interface and the ease of carrier transmission through the interface. Generally, smooth boundaries lead to a higher κ compared with rough boundaries because a rough boundaries are more likely to reverse phonon momentum, thus impeding heat transfer and reducing κ_{ph}.[70–72] Boundary scattering is important at low T and in nanostructures.

Three-phonon scattering processes can be divided into normal scattering and Umklapp scattering. In both scattering processes, two phonons can combine to produce a third phonon, or a phonon can split into two phonons. In normal scattering processes, the wavevectors ($\boldsymbol{k}$) of all phonons involved remain inside the first Brillouin zone, in which both energy and momentum are conserved. Thus, normal scattering only brings about the redistribution of phonon momentum and usually has no impact on κ. On the other hand, the $\boldsymbol{k}$ of a scattered phonon in an Umklapp process falls outside of the first Brillouin zone. Such a phonon with a large $\boldsymbol{k}$ is meaningless in physics due to the discrete nature of the atomic lattice. The $\boldsymbol{k}$ should be mathematically transformed to a point inside the first Brillouin zone by a reciprocal lattice vector. As such, Umklapp scattering does not conserve momentum, which leads to thermal resistance. Umklapp scattering is the dominant phonon scattering mechanism at high T.

Lattice imperfection scattering happens due to a substitution of a foreign atom at a lattice site, an interstitial atom placed in the lattice, or the presence of vacancies, whereas the spring constants and the mass of the lattice sites are changed. The theory of lattice imperfection scattering was put forward by Klemens in 1955.[73] Using the second-order perturbation, frequency dependence of phonons for different imperfections was established.

Electron-phonon scattering involves one phonon and two electrons. An electron either absorbs or emits a phonon, and changes its trajectory. In general, the electron-phonon scattering becomes important in materials with a high electron concentration.[74,75]

2. Electron

Electrons are charged subatomic particles, which act as the primary carriers of electricity in solids. The electronic specific heat follows a linear T dependence at low T. In a solid, electrons mainly participate in four scattering processes: electron-impurity scattering, electron-phonon scattering, electron-electron scattering and electron-boundary scattering.

Electron-impurity scattering can be described as the interaction between electron flow and impurities or lattice defects. This interaction is usually the dominant scattering mechanism at low T. Moreover, since the masses of impurities are normally much larger than those of electrons, they cannot absorb or provide energy to the colliding electrons, and the energy of electrons does not change during the whole collision. Therefore, electron-impurity scattering is considered as a purely elastic interaction.

The deflection of electrons from their original paths due to the interference produced by vibrating ions can be considered as electron-phonon scattering. In contrast to electron-impurity scattering, this interaction includes the emission or absorption of phonons, which can cause small but non-negligible energy changes in the electrons, so it cannot be treated as purely elastic scattering. In addition, electron-phonon scattering can be divided into two types of processes: normal process and Umklapp process. For normal process, collisions between phonons and electrons follow the conservation law of momentum. Regarding Umklapp process, this is the main mechanism at high T that can effectively generate resistance because it almost reverses the direction of the electron $\boldsymbol{k}$.

Electron-electron scattering is an important scattering mechanism in very pure metals at ultra-low T. In this interaction, four electron states are involved: two initial states that undergo scattering and two states in which electrons are scattered.[76] Similar to electron-phonon scattering, electron-electron scattering includes both normal and Umklapp processes, but the Umklapp process occurs

under the stringent conditions specified by the Pauli exclusion principle. Therefore, in bulk metals, the transport effects contributed by electron-electron scattering can be neglected at room temperature. A low T, the resistivity determined by the 3D electron-electron scattering rate follows a quadratic T dependence.

Electron-boundary scattering can occur at the metal/metal interfaces or dielectric/metal interfaces and lead to thermal boundary resistance. At the metal/metal interfaces, the thermal boundary resistance is expected to be determined by the electrons since the Fermi velocity of the electrons in most metals is several orders of magnitude larger than the phonon group velocity.[77] At the dielectric/metal interfaces, this scattering process is mediated by heat transfer from electrons on the metal side to phonons on the dielectric side.[77]

Electronic contribution to κ is related to electrical conductivity (σ) via the Wiedemann-Franz (WF) law as

$$\frac{\kappa_e}{\sigma} = LT,$$

where L is the Lorenz number. The Sommerfeld value of Lorenz number is $L_0 = 2.45 \times 10^{-8}$ $V^2 K^{-2}$. In general, the WF law is valid when electron and heat currents follow the same underlying scattering mechanism with only weak energy dependence. However, violations of the WF law have also been reported in some strong-correlated systems.[78–80]

3. Magnon

Magnons are collective excitations of electron spin structure in magnetic materials (Fig. 1b). In some magnetic materials, the contribution of magnons to thermal transport is comparable to that of phonons.[81] Similar to phonons, magnon scattering mechanisms also include magnon-phonon scattering, magnon-defect scattering, multi-magnon scattering and magnon-electron scattering.

Magnon-phonon scattering is caused by spin-orbital coupling,[82] and can be divided into two types at the lowest order: radiation process (R-process) and conversion process (C-process).[83] In R-processes, one magnon is created and the other is annihilated. In C-processes, magnons are either created or annihilated due to phonon emission or absorption.

Magnons can also be scattered by point defects and grain boundaries.[84] These imperfections can lead to variations or reductions in spin-spin interaction, resulting in a reduced magnon MFP. It has been found that even weak dislocation-like defects can act as strong grain boundaries for magnon propagation, reducing magnon thermal conductivity.[85]

Multi-magnon scattering includes three-magnon scattering and four-magnon scattering. Three-magnon scattering can be described as a magnon splitting into two magnons, or two magnons combining to produce a third magnon. Four-magnon scattering is the annihilation of two magnons with $\boldsymbol{k} = 0$ and the creation of two magnons with finite and opposite $\boldsymbol{k}$.[86] During this process, the initial energy excess of the modes with $\boldsymbol{k} = 0$ is transferred to the magnons with $\boldsymbol{k} \neq 0$, while the total energy of magnetic system is conserved.

The scattering of magnons by mobile electrons or holes is also important for magnetic heat transport. It has been found that the magnitude of magnon thermal conductivity is highly sensitive to the charge carrier concentration in some magnetic materials.[81,87]

The interaction between magnons and phonons is necessary for observing κ_{spin}. The magnon-phonon thermal diffusion process can be treated with a two-temperature model,[88,89] where the temperatures of magnons and phonons are considered as two separate systems with their own

temperature gradient. The energy transfer between them is proportional to the temperature difference. The two-temperature model can explain the phenomenon in which a system with strong magnon-phonon coupling exhibits similar phonon and magnon equilibrium temperatures. Additionally, the two-temperature model predicts an effective thermal conductivity that is closer to the sum of the magnon and phonon thermal conductivity contributions.

4. Spinons

Spinons are one of three quasi-particles split from electron in solids during spin-charge separation, the other two being holons and orbitons. Although both magnons and spinons can be considered collective spin excitations, they possess different spin numbers. Magnons have a spin of 1 while spinons have a spin of $1/2$. Therefore, magnons are bosons and follow Bose-Einstein statistics, and spinons are fermions who follow Fermi-Dirac statistics. Spinons are important elementary excitations in 1D spin chains and QSLs.[2] In a spin-$1/2$ 1-D antiferromagnetic (AFM) chain, a spin-flip excitation will reorientate one spin into a ferromagnet order with its neighboring spins, forming one $S = 1$ magnon with two domain walls. The unfavorable ferromagnet coupling leads to the flip of neighboring spins, pushing the domain walls outwards.[90,91] Such domain wall excitations in the 1-D AFM chain are called spinons.

The spinon heat transport in the spin-1/2 1-D AFM chain has a ballistic nature.[92,93] As a result of the integrability of spin chains, intrinsic spinon-spinon coupling alone is not resistive for magnetic heat transport. However, finite κ_{spin} has been observed in several spin chain compounds, which is due to the scattering of spinons by defects, grain boundaries and phonons.[94]

It has been found that the spinon-defect scattering plays an important role in spinon thermal transport at low T, where the reduction of impurity concentrations can exceptionally enhance κ_{spin}.[95–97] At high T, the spinon-phonon Umklapp process dominates the thermal transport process, which causes a significant reduction in κ_{spin}.

B. Kinetic theory of thermal transport

In quantum materials, heat is not only carried by electrons but also by charge-neutral quasi-particles. In general, kinetic theory[98] can be used to describe the thermal transport mediated by these heat carriers as

$$\kappa = \frac{1}{3} C v l,$$

where v is the average velocity of heat carriers, and l is their MFP, which is related to the average scattering time (τ) as $l = v\tau$.[99]

Matthiessen's rule,[100] derived from the work of Augustus Matthiessen in 1864, has been used to describe the combined effect of multiple independent scattering processes. Therefore, the scattering time can be expressed as

$$\frac{1}{\tau} = \frac{1}{\tau_D} + \frac{1}{\tau_U} + \frac{1}{\tau_B} + \ldots,$$

where τ_D, τ_U and τ_B are the relaxation time due to defect scattering, Umklapp process and boundary scattering, respectively.

C. Thermal characterization methods

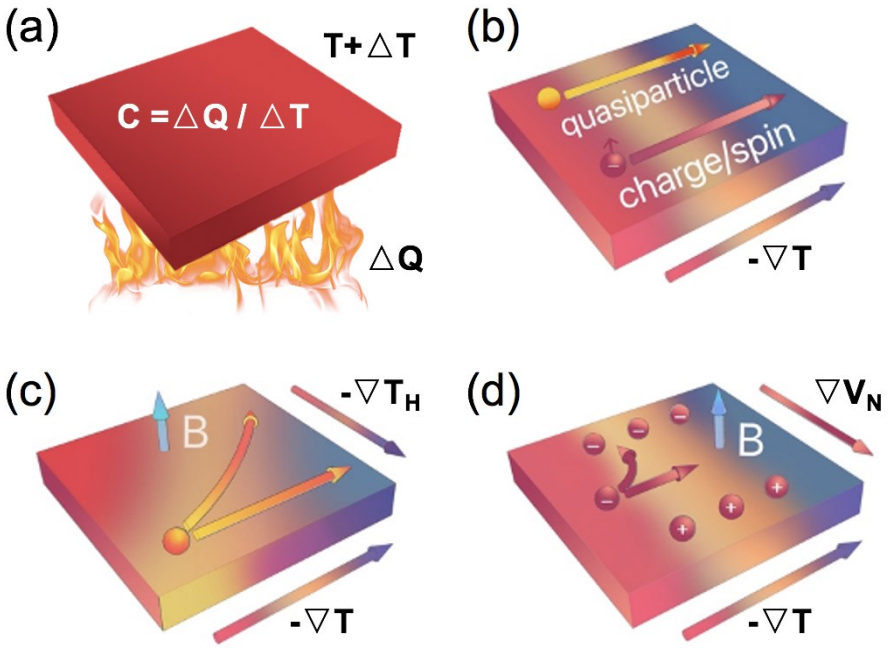

Figure. 2: *Schematic diagrams of several thermal characterization methods: (a) specific heat, (b) thermal conductivity, (c) thermal Hall effect, and (d) Nernst effect.*

Fig. 2 illustrates several thermal characterization methods, including specific heat, thermal conductivity, THE, and Nernst effect measurements. Specific heat is defined as the quantity of heat required to raise the temperature of one gram of a substance by one Celsius degree (Fig. 2a). Both itinerant and localized excitations can contribute to specific heat. Therefore, this measurement can be used to detect the evolution of entropy in quantum materials, such as phase transitions. There are several methods to measure specific heat, including differential scanning calorimetry (DSC) and adiabatic calorimetry.

The κ of a material is a measure of its ability to conduct heat (Fig. 2b). The thermal conduction is governed by Fourier's law:

$$\begin{pmatrix} j_x \\ j_y \end{pmatrix} = \begin{pmatrix} -P/(t_s \cdot w_s) \\ 0 \end{pmatrix} = \begin{pmatrix} \kappa_{xx} & \kappa_{xy} \\ -\kappa_{xy} & \kappa_{yy} \end{pmatrix} \begin{pmatrix} -\Delta T_x/l_s \\ -\Delta T_y/w_s \end{pmatrix},$$

where j_x and j_y are the heat currents along the longitudinal and transverse directions, separately, P is the applied heat power, l_s is the length between the two longitudinal thermometers, w_s is the sample width, t_s is the sample thickness, κ_{xx} is the longitudinal thermal conductivity, ΔT_x is the longitudinal temperature difference between heater and cold finger, and ΔT_y is the transverse temperature difference. Therefore, κ_{xx} can be expressed as:

$$\kappa_{xx} = \frac{P l_s}{\Delta T_x w_s t_s}.$$

κ measurements are a powerful tool in probing the thermal transport properties of quantum materials, including types of heat carriers, scattering mechanisms, and coupling between heat carriers. Two common techniques for measuring κ of bulk materials are the steady-state and transient methods.[101] In these two methods, a sample is placed between a heat source and a heat sink. The major difference is that the steady-state method utilizes a steady-state heat flow while the transient method utilizes a pulsed or periodic heat source. Recently, several new techniques have been developed to measure the κ of nanostructured materials, including time domain thermo-

reflectance (TDTR),[102,103] suspended micro-bridge,[104,105] optothermal Raman technique[106–109] and scanning thermal microscopy (SThM).[110–113]

Analogously to electronic Hall conductivity, a longitudinal temperature gradient (∇T) induces a transverse heat flow under a magnetic field (B) applied along the third perpendicular direction (B_z), as shown in Fig. 2c. Therefore, κ_{xy}, which can be induced by electrons, phonons, or spin excitations, is powerful for probing the topological properties and novel quantum phases of quantum materials. κ_{xy} can be written as:

$$\kappa_{xy} = \kappa_{yy} \frac{\Delta T_y / w_s}{\Delta T_x / l_s},$$

where $\kappa_{yy} = \kappa_{xx} = \kappa$ in isotropic materials.

The Nernst effect is a thermoelectric phenomenon observed in electrically conductive materials. A transverse electric field (E_y) can be generated when a ∇T and an external B are applied in the longitudinal and third vertical directions, respectively (Fig. 2d). Additionally, if a material exhibits spontaneous magnetization, the transverse electrical field can be measured without an external B. Such a phenomenon is called anomalous Nernst effect. By introducing Nernst coefficient ($|N|$), Nernst effect can be expressed as

$$|N| = \frac{(E_y / B_z)}{\nabla T}.$$

In addition, the Nernst thermopower (S_{xy}) can be obtained as

$$S_{xy} = \frac{E_y}{\nabla T}.$$

The Nernst effect measurement can be used to study the topological nature of materials due to its sensitivity to the Berry curvature near the Fermi level.

D. Berry curvature theory

Since Berry curvature is highly related to the THE and ANE, we introduce Berry curvature theory briefly in this section. The Berry phase is a quantum phase effect that emerges during the adiabatic evolution of a quantum state.[114] Berry curvature is an anti-symmetric second-rank tensor, which can be regarded as a local gauge field connected to Berry phase through the Kelvin–Stokes theorem.

1. Berry curvature and THE

Berry curvature has a direct effect on various THEs because it behaves like B and thus imparts anomalous velocities perpendicular to the thermal potential to heat carriers. By applying the approach of semiclassical wave packet dynamics, the general formula of κ_{xy} for various systems such as electrons, phonons, and magnons is obtained,[114] and the relationship between Berry curvature and κ_{xy} is also manifested naturally, which can be expressed as[115]

$$\kappa_{xy} = -\frac{\partial \boldsymbol{J}_{Qx}^{tr}}{\partial_y T} = \frac{\partial \boldsymbol{M}_Q^{ed}}{\partial T} = \frac{2\pi}{VhT} \sum_{n,\boldsymbol{k}} [\int_{\varepsilon_{n(\boldsymbol{k})}}^{\infty} (\epsilon - \mu)^2 \frac{\partial f}{\partial \epsilon} d\epsilon] \boldsymbol{\Omega}_n(\boldsymbol{k}),$$

where $\boldsymbol{J}_{Qx}^{tr}$ is the transport current along the x-axis, $\boldsymbol{M}_Q^{ed}$ is the thermal magnetization at the edge, ε_n is the energy of the nth Bloch band, μ is the chemical potential and $\boldsymbol{\Omega}_n$ is the Berry curvature of the nth band in the 3D parameter space. It can be seen that the magnitude of κ_{xy} is proportional to $\boldsymbol{\Omega}_n$. Furthermore, the combined formula of the three conductivities (AHE σ_H, thermal Hall

electronic conductivity σ_T, and κ_{xy}) has also been obtained[115]

$$\sigma, \kappa = \frac{2\pi(-e)^{2-m}}{VhT^{\alpha}} \sum_{n,\boldsymbol{k}} [\int_{\varepsilon_n(\boldsymbol{k})}^{\infty} (\epsilon - \mu)^m \frac{\partial f}{\partial \epsilon} d\epsilon] \boldsymbol{\Omega}_n(\boldsymbol{k}) = -\frac{2\pi e^{2-m}}{VhT^{\alpha}} (k_B T)^m \sum_{n,\boldsymbol{k}} F_m(\varepsilon_n(\boldsymbol{k})) \boldsymbol{\Omega}_n(\boldsymbol{k}),$$

$$F_m(\varepsilon_n) = \int_0^{f(\varepsilon_n)} [log(\rho^{-1} - 1)]^m d\rho,$$

where $F_m(\varepsilon_n)$ is a weighting function, α and m equal to 0 correspond to σ_H, α and m equal to 1 correspond to σ_T, and $\alpha = 1$ and $m = 2$ correspond to κ_{xy}.

2. Berry curvature and anomalous Nernst effect

Recent studies have shown that the ANE is a symbol of Berry curvature neighboring the Fermi level, especially in topological Weyl semimetals.[116–119] The physical origin of the ANE is similar to the AHE, where the AHE is a Hall signal occurring without external B. In $\boldsymbol{k}$-space, the ANE can be expressed as

$$\alpha_{yx}^{A} = \frac{2\pi k_B e}{h} \sum_n \int \frac{d^3\boldsymbol{k}}{(2\pi)^3} \boldsymbol{\Omega}_{n,z}(\boldsymbol{k}) s_{n,\boldsymbol{k}}.$$

where $s_{n,\boldsymbol{k}}$ is the occupational entropy, which is non-zero in partially filled bands, α_{yx}^{A} is the anomalous transverse thermoelectric conductivity, and $\boldsymbol{\Omega}_{n,z}(\boldsymbol{k})$ is the portion of Berry curvature along the third vertical direction, which acts similarly to an external B.[117] Although the ANE and AHE are commonly seen as sister effects, there are still important distinctions between the two. The ANE is sensitive to Berry curvature close to the Fermi level while the AHE is related to the sum of Berry curvature of all occupied bands.[116,120]

III. EXAMPLES OF THERMAL CHARACTERIZATION AS A USEFUL PROBE OF QUANTUM MATERIALS

A. Thermal characterization as probe of QSLs

QSLs are formed by interacting quantum spins in certain magnetic materials, in which strong quantum fluctuations prevent long-range magnetic ordering. They are a novel class of condensed-matter phase with a variety of exotic physical properties arising from their topological characters, such as long-range quantum entanglement, fractionalized excitations and absence of ordinary magnetic order even at 0 K.[17,52,53] It is currently difficult to probe the lacking of the magnetic order in QSLs directly. In practice, multiple techniques, such as neutron scattering, resonant X-ray scattering, specific heat, magnetic susceptibility, nuclear magnetic resonance (NMR) spectroscopy, optics must be used to characterize QSLs. When a magnet harbors a QSL state, heat is carried not only by magnons and phonons as conventional insulating magnets, but also spinons and other spin excitations, making thermal transport an important probe for characterizing QSLs.[17,121,122] One advantage of probing QSL states by κ measurements is that these measurements are free from a direct impurity spin fluctuation contribution. Impurities always act as scattering sources in thermal transport. In comparison, impurity spins in inelastic neutron scattering and NMR measurements contribute directly to the signal.[121,122,123]

The organic Mott insulator $EtMe_3Sb[Pd(dmit)_2]_2$ with a 2D triangular lattice (Fig. 3a) is a

promising QSL candidate.[124–128] However, there is still debate over whether mobile gapless excitations, a sign of a QSL, can be detected in this material.[129–131] At low T, both acoustic phonons and itinerant spin excitations can contribute to the thermal transport in $EtMe_3Sb[Pd(dmit)_2]_2$ as $\kappa = \kappa_{ph} + \kappa_{spin}$. Therefore, as κ_{ph}/T disappears at 0 K, the observation of a finite linear residual κ ($\kappa_0/T = \lim_{T\to 0} \kappa/T$) can support the presence of the itinerant gapless spin excitations. Fig. 3b summarizes the reported κ data of $EtMe_3Sb[Pd(dmit)_2]_2$ by several research groups.[124,129–133] Among them, sample A and B are reported by Yamashita *et al*. in 2010. A sizable residual linear term can be observed.[124] However, Bourgeois-Hope *et al*. followed the same sample preparation method, and got much smaller κ values (samples C, D and E).[129] On the one hand, samples A and B show an upward curvature, while samples C, D and E show a downward sublinear curvature. On the other hand, following T^2 fitting, the residual linear terms of samples A and B are almost 1.9 and 1.1 mW K^{-2} cm^{-1}, respectively, which are $50-100$ times larger than those of samples C, D and E. Ni *et al*. performed similar κ measurements (samples F and G),[130] which are consistent with the data reported by Bourgeois-Hope *et al*. In addition, the relationship between κ/T and B are different for reported measurement data. As shown in Fig. 3c, the results from Bourgeois-Hope *et al*. and Ni *et al*. both show that κ is nearly independent of B while the data from Yamashita *et al*. increase with B.[124,129,130] Until recently, Yamashita *et al*. found that the cooling rate may affect κ measurements.[131] As shown in Fig. 3d, a finite linear residual κ can be observed under slow-cooling conditions (samples 1 and 3), but disappears under rapid-cooling conditions (samples 4 and 5). However, a comparison of samples 2 and 5 show that nearly identical cooling rates lead to different results. Such a discrepancy was attributed to random scatterers introduced during the cooling process.

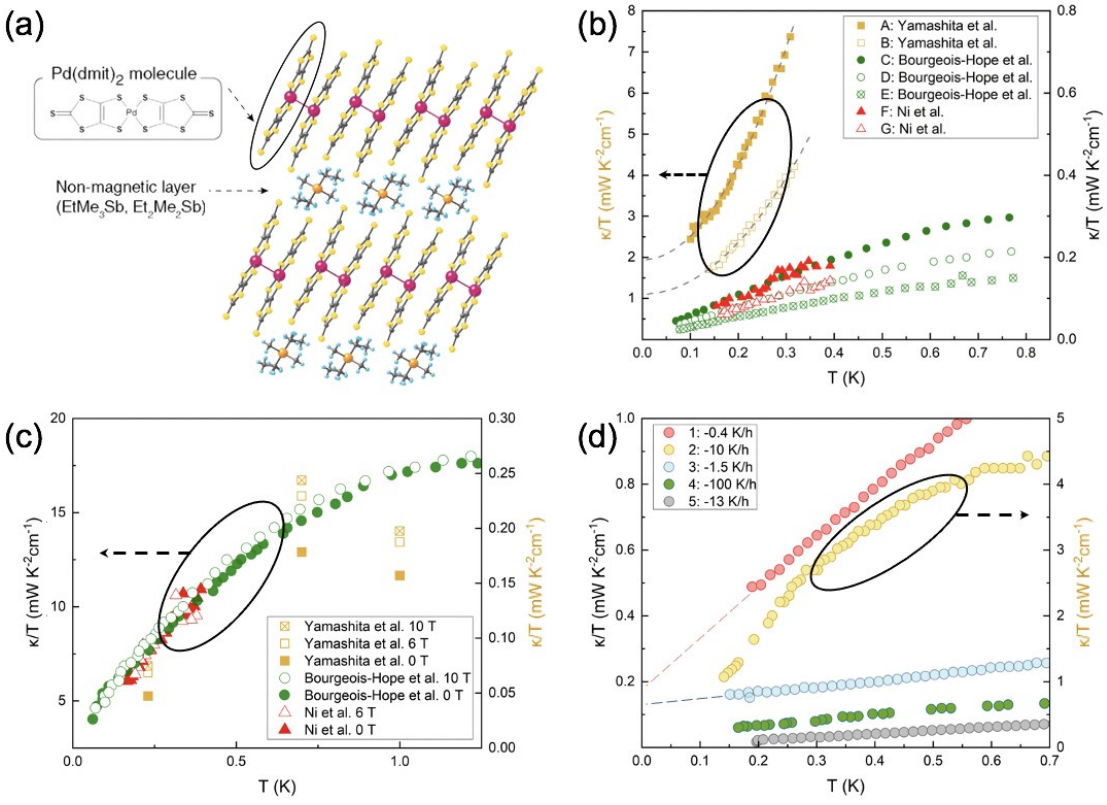

Figure. 3: *(a) Crystal structure of $EtMe_3Sb[Pd(dmit)_2]_2$. (b) T dependence of κ/T.*[124,129,130] *Two gray dashed lines*

are fitting results with T^2. (c) T dependence of κ/T under different B.[124,129,130] *(d) T dependence of κ/T under different cooling rate. Two dashed lines show the extrapolation of sample 1 and 3 plotted as a function of T.* [124,131,133] *Fig. 3a reproduced with permission from Science. 328, 1246–1248 (2010).*[124] *Copyright 2010 American Association for the Advancement of Science.*

α-$RuCl_3$ is an insulating 2D quantum magnet (Fig. 4a) with a dominant Kitaev interaction on a 2D honeycomb lattice.[134] This material is a good candidate for realizing the Kitaev spin liquid (KSL).[54,135–137] As shown in Fig. 4b, AFM order is destroyed by in-plane magnetic field and a QSL state emerges.[138,139] Elementary excitations in the Kitaev model can be divided into two types of Majorana fermions: localized Z_2 fluxes with gap and itinerant fermions. The neutral itinerant Majorana fermions can be detected from κ_{xy} measurement because while they are not affected by electric field, they can carry heat due to Majorana-phonon coupling.[140] The experimental observation of quantization of κ_{xy} was reported by Kasahara *et al*.[54] As shown in Fig. 4c, κ_{xy}/T shows a plateau in the range of $\sim 4.5\ \mathrm{T} < \mu_0 B_\perp < \sim 5.0\ \mathrm{T}$. The value of this plateau approximately coincides with the half of the thermal Hall conductivity per 2D sheet (κ_{xy}^{2D}) in the quantum Hall state [141] given by

$$\kappa_{xy}^{2D}/T = q(\pi/6)(k_B^2/\hbar),$$

where coefficient q provides the chiral central charge of the gapless boundary modes. This half-integer quantization suggests the presence of charge-neutral Majorana fermions. A recent study by the same group found that the half-integer thermal Hall plateau occurs even for B with no out-of-plane components (Fig. 4d).[138] The observed sign structure of the measured B-angular variation of QHE is consistent with the topological Chern number of the pure KSL (Fig. 4e).[138] The results suggest the formation of non-Abelian topological order associated with fractionalization of the local magnetic moments in α-$RuCl_3$. Furthermore, when a B is applied along the a-axis, there is an abrupt change of κ and C, indicating a first-order phase transition separating two QSL states with different Chern numbers.[142]

Recently, a periodic oscillation of κ in the QSL state of α-$RuCl_3$ below 1.74 K has been observed by Czajka *et al*.[139] The oscillation is prominent in QSL state and vanishes in zigzag and polarized state. This behavior could be explained by the quantization of the spinon Fermi surface similar to Shubnikov de Haas oscillations in metals.[143] It is noted that another work by Bruin *et al*. suggested that the oscillatory features in κ is due to field-induced phase transitions rather than from quantum oscillations.[144] The κ_{xy} data from Czajka *et al*. show similar trends as those reported by Yokoi *et al*.[138] However, a strong T dependence of κ_{xy} was observed, which is inconsistent with the quantized value appearing in the interval $3.8 - 6$ K. Moreover, the similarity between the T dependence of κ_{xy} and phonon-dominated κ_{xx}, observed by Hentrich *et al*.[145] and Lefrançois *et al*.[146] show that instead of Majorana fermions, κ_{xy} in α-$RuCl_3$ should be attributed to phonons. Therefore, further studies are needed to better understand the κ_{xy} data of α-$RuCl_3$. Thermal measurements can be combined with precise theoretical models and other measurement techniques to probe the possible QSLs.

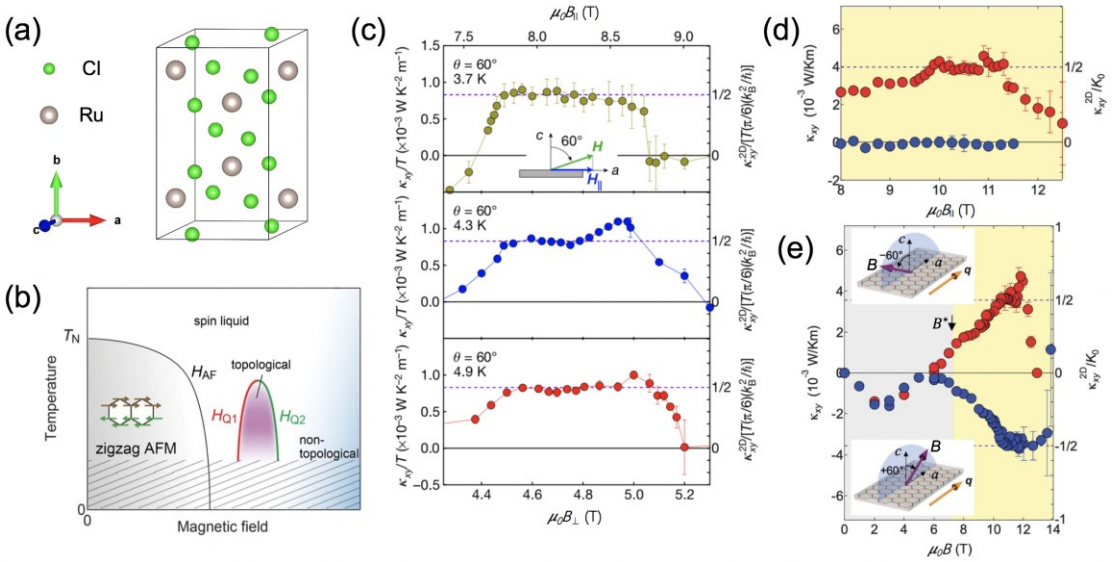

Figure. 4: *(a) Crystal structure of α-$RuCl_3$. (b) Magnetic phase diagram of α-$RuCl_3$ under magnetic field. (c)B dependence of κ_{xy} in tilted-B of 60° away from c-axis at different T. Violet dashed lines represent half-integer-κ_{xy}. (d) κ_{xy} in paramagnetic state for $B||-a$ axis (red circles) and $B||b$ axis (blue circles) at 4.8 K with no out-of B component. (e) B dependence of κ_{xy} at 4.3 K in tilted$-B$ of $-60°$and 60° away from c-axis. Gray and yellow shaded areas represent AFM-ordered and QSL states, respectively. Fig. 4c reproduced with permission from Nature 559, 227–231 (2018).*[54] *Copyright 2018 Springer Nature. Fig. 4b, 4d and 4e reproduced with permission from Science. 373, 568 (2021).*[138] *Copyright 2021 American Association for the Advancement of Science.*

In addition to κ and κ_{xy}, C can also provide useful information about the QSL state in α-$RuCl_3$. $C(T)$ in the KSL is predicted to exhibit two-peak characteristics because two types of fermions release entropy at distinctly different T.[55,147–149] However, experimental realization of this $C(T)$ behavior in α-$RuCl_3$ is complicated due to the reliable subtraction of the phonon background and a structural phase transition at about 160 K.[150,151] Widmann *et al*. estimated the phonon background by measuring a nonmagnetic $RhCl_3$ with an identical crystal structure to α-$RuCl_3$ together with *ab initio* calculations.[152] Fig. 5a shows the $C(T)$ of α-$RuCl_3$ and $RhCl_3$. The magnetic C of α-$RuCl_3$ at different B can be extracted by subtracting the phonon background, as shown in Fig. 5b. At 0 T, the anomaly at 6 K is due to the magnetic phase transition and the broad hump at 70 K can be attributed to the release of entropy from itinerant Majorana fermions. This T corresponds to the theoretical Kitaev interaction of 80 K.[153] As B increases, long-range spin order is suppressed, where the peak around 6 K decreases and is approximately smooth at 9 T. Therefore, the C measurement proves that KSL is a stable state in α-$RuCl_3$ at elevated T in a broad range of B. Recently, Tanaka *et al.* measured the C for different in-plane rotations of an applied B, and provided evidence for filed-angle-dependent Majorana gap in α-$RuCl_3$. [154]

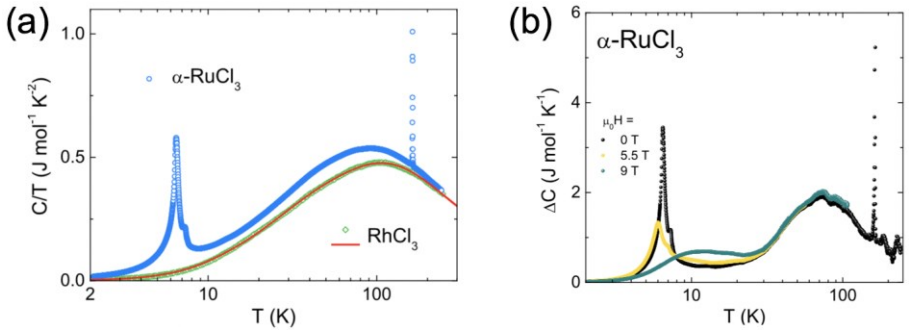

Figure. 5: *(a) T dependence of the C for α-$RuCl_3$ and $RhCl_3$. Red solid line: the C of $RhCl_3$ calculated based on the Debye-Einstein model. (b) T dependence of the excess C of α-$RuCl_3$ under different in-plane B. Fig. 5a and 5b reproduced with permission from Phys. Rev. B 99, 094415 (2019).*[152] *Copyright 2019 American Physical Society.*

B. Thermal characterization as probe of Berry curvature

Berry curvature, which acts like a magnetic field in ***k***-space, is an intrinsic mechanism for the THE of charge-neutral excitations such as phonons and spin excitations. Berry curvature can give heat carriers anomalous velocities perpendicular to ∇T, and makes heat current deflect to the left or right like electrons under Lorentz force.[114,155–159] To address the major challenge of distinguishing phonon and magnon contributions to the κ_{xy} of magnetic insulators, detailed analysis of temperature and field dependence of κ_{xx} and κ_{xy} is needed.

The magnon Hall effect has been detected on the ferromagnetic insulator $Lu_2V_2O_7$ by Onose *et al*. in 2010 and attributed to the Dzyaloshinskii-Moriya interaction, which originates from the spin-orbit coupling and is seen as one of the sources leading to the non-zero magnonic Berry curvature.[160] The κ_{xy} decreases with B, contradicting the phonon mechanism in which the κ_{xy} should increase with B due to reduced spin-phonon scattering. Recently, Hirschberger *et al*. measured a large κ_{xy} in the kagome magnet Cu(1-3, bdc) (Fig. 6a), which not only relates κ_{xy} to the Berry curvature, but also attributes the apparent sign reversal of κ_{xy} to the sign alternation of the Chern flux between magnon bands.[161] As shown in Fig. 6b, above the ordering temperature of 1.8 K, κ_{xy} displays a nonmonotonic B dependence, where κ_{xy} peaks at low B, and exhibits a zero crossing at higher B (curve at 2.78 K). Below the ordering temperature, the sign of κ_{xy} is reversed (curves at 1.74 and 0.82 K). The spin thermal conductivity κ_{xx}^{s} (Fig. 6c), which is extracted from field-dependent part of κ_{xx}, and κ_{xy} (Fig. 6d), shows a similar exponential decrease with temperature at large B. This finding results from the suppression of the magnon population from the Zeeman gap, and therefore rules out the phonon origin. These phenomena are also reproduced in theoretical calculations based on the Holstein-Primakoff and Schwinger-boson mean-field theories, where κ_{xy} and Berry curvature are directly related in these two theories.[162] Therefore, the appearance of κ_{xy} can be interpreted as the Berry curvature imparting an anomalous velocity to magnons.

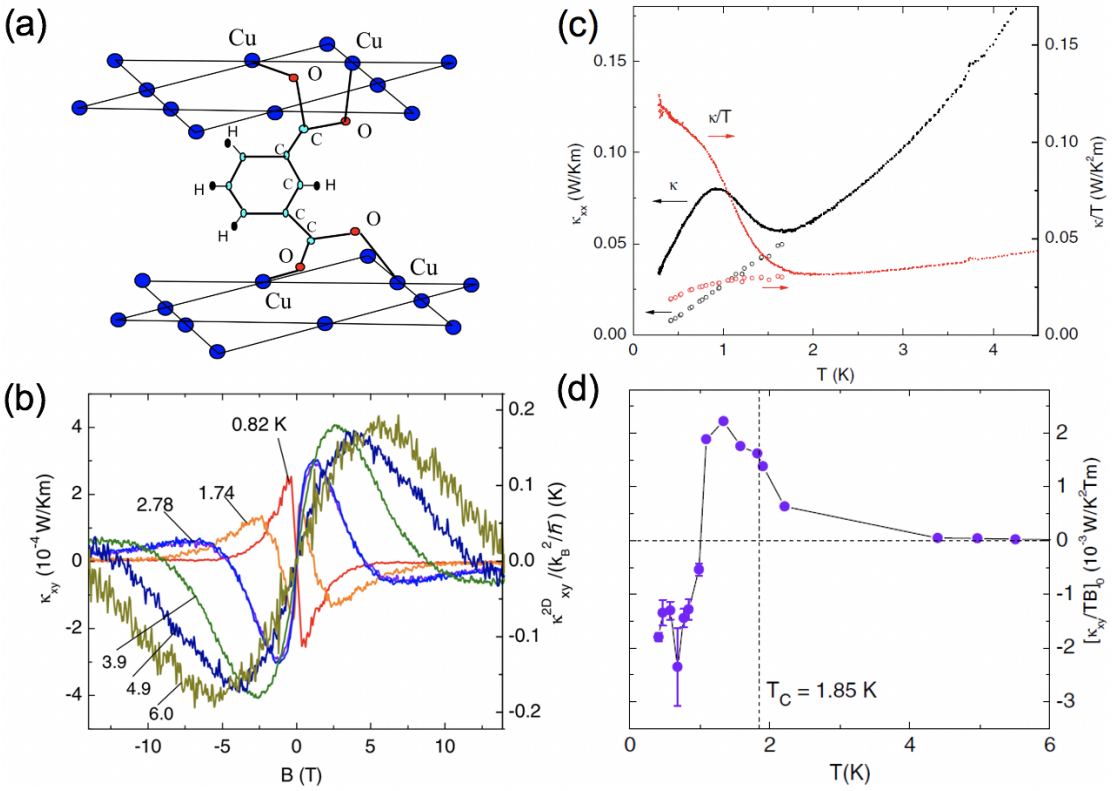

Figure. 6: *(a) Crystal structure of Cu(1-3, bdc). (b) B dependence of* κ_{xy}/T *and* κ^{2D}_{xy} *at different T. (c)* κ *(black symbols) and* κ/T *(red) for* $T < 4.5$ *K. Values of* κ *and* κ/T *at large B (identified with the phonon background) are shown as open symbols. (d) T dependence of the quantity* $[\kappa_{xy}/TB]_0$ *which measures the thermal Hall response in the limit* $B \rightarrow 0$*. Fig. 6a reproduced with permission from Phys. Rev. B 80, 132402 (2009).*[163] *Copyright 2015 American Physical Society. Fig. 6b, c, d reproduced with permission from Phys. Rev. Lett. 115, 106603 (2015).*[161] *Copyright 2015 American Physical Society.*

Large κ_{xy} was also discovered in the frustrated magnet $Tb_2Ti_2O_7$ and attributed to spin excitations.[164] However, Hirokane *et al.* replaced 70% of the magnetic Tb^{3+} by non-magnetic Y^{3+} and discovered an even larger κ_{xy}, ruling out the magnetic excitation origin and supporting the phonon origin.[165]

Furthermore, the ANE can be treated as a signature for the Berry curvature near the Fermi level in the topological Weyl semimetals. Weyl semimetals are materials where the valence and conduction bands intersect at single points, called the Weyl nodes.[166–168] For example, a giant ANE in $Co_3Sn_2S_2$ (Fig. 7a) was reported by Yang *et al.*, and was resulted from the nontrivial Berry curvature close to the chiral Weyl points.[61] As shown in Fig. 7b, the S_{xy} in $Co_3Sn_2S_2$ exhibits the largest maximum value at extremely low magnetization compared to the previous magnetic materials (blue-shaded area), which strongly violates the traditional scaling relationship in conventional ferromagnets. Similar phenomena also occur in $CoMnGa_2$ and the topological chiral antiferromagnet Mn_3Sn.[169] In addition, the ratio of anomalous Nernst signal to the magnetization $|S^A_{xy}|/\mu_0 M$ (Fig. 7c) for these topological Weyl semimetals is much higher than that of the trivial ferromagnetic materials.[169] This finding not only indicates that the transverse signal is significantly stronger in the topological Weyl semimetals, but also implies that the anomalous transport properties are due to the presence of Weyl nodes, which are monopole-like singularities of the Berry curvature.

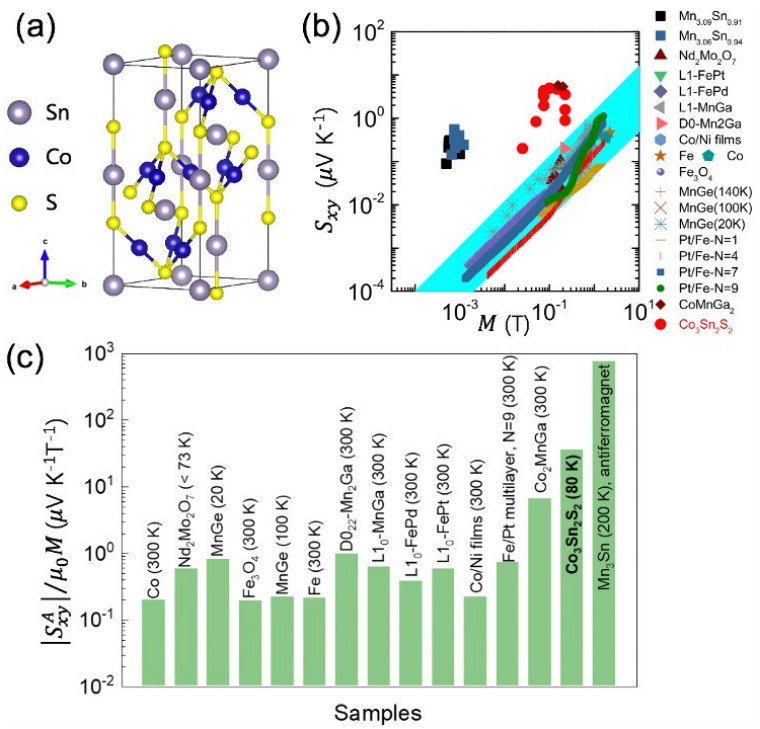

Figure. 7: *(a) Crystal structure of $Co_3Sn_2S_2$. (b) Magnetization dependence of the spontaneous Nernst effect for Mn_3Sn, $Co_3Sn_2S_2$ and various ferromagnets. (c) Comparison of ratio of anomalous Nernst signal to the magnetization for Mn_3Sn, $Co_3Sn_2S_2$ and various ferromagnets. Fig. 7b reproduced with permission from Phys. Rev. Mater. 4, 024202 (2020).*[61] *Copyright 2020 American Physical Society. Fig. 7c reproduced with permission from Adv. Mater. 31, 1806622 (2019).*[169] *Copyright 2019 John Wiley & Sons.*

C. Thermal characterization as probe of chiral anomaly

In Weyl semimetals, electrons follow the relativistic equations of motion for gravitational forces and electron dynamics.[170] Chiral anomalies were predicted as an experimental signal for the existence of Weyl semimetals four decades ago.[171] When parallel electric and magnetic fields are applied to an ideal Weyl semimetals, the chiral symmetry of monopoles with opposite chirality ($\chi = \pm 1$) is broken. Although negative longitudinal magnetoresistance was considered as a valid signature,[172] the interpretation becomes vague because the Lorentz force can distort the spatial distribution of current flow under applied B.[173] Recently, Vu *et al*. discovered thermal chiral anomalies in the B-induced ideal Weyl semimetals state of $Bi_{1-x}Sb_x$.[174] Fig. 8a illustrates the energy dispersion of a field-induced Weyl semimetals, where the degeneracy of the Kramers doublets (W points) is enhanced by the Zeeman energy. As shown in Fig. 8b and c, the κ of $Bi_{95}Sb_5$ in a non-Weyl phase is always negatively proportional to B, while the κ of $Bi_{89}Sb_{11}$ after becoming an ideal Weyl semimetal at $B > 1 - 2$ T exhibits a strong uptrend. This finding results from energy pumping between opposite chirality monopoles when a thermal gradient is applied parallel to a magnetic field in an ideal Weyl semimetal. A strong enhancement of κ is related to the enhanced κ_e due to the excess σ as a result of charge pumping. Additionally, the authors have confirmed the robustness of the experimental observations with respect to defect and phonon scattering.

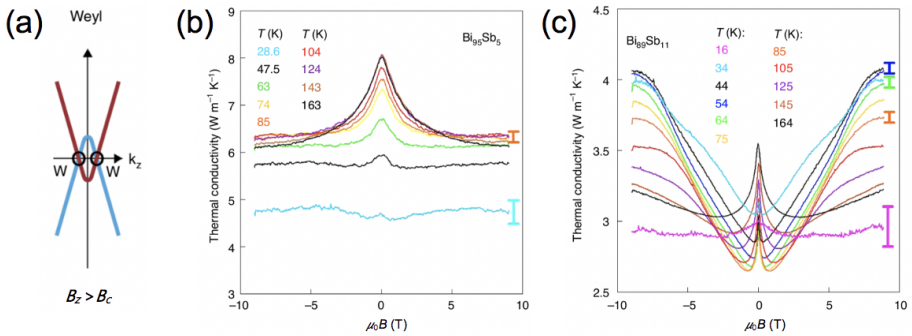

Figure. 8: *(a) Electronic band structure of B-induced Weyl semimetals, where B_z (applied-B along the z-axis) is greater than critical threshold B_c. (b) and (c) B dependence of κ for $Bi_{95}Sb_5$ and $Bi_{89}Sb_{11}$ along the $< 001 >$ direction. Fig. 8a, 8b and 8c reproduced with permission from Nat. Mater. 20, 1525–1531 (2021).*[174] *Copyright 2021 Springer Nature.*

Xiang *et al*. observed huge magnetic quantum oscillations (MQOs) in the $\kappa(B)$ of another Weyl semimetal TaAs (Fig. 9a). The MQOs were attributed to the newly proposed chiral zero sound (CZS),[175] which is a collective bosonic excitation of Weyl fermions. As shown in Fig. 9b, the amplitude of MQOs in $\kappa_{\parallel}(B)$ has become remarkably large in the last MQO period and is about $3-4$ times of $\kappa_{\parallel}(B=0)$. Compared with the κ_e estimated from the WF law ($\kappa_{e,WF}$), the oscillation amplitude of $\kappa_{\parallel}(B)$ is not only 2 orders of magnitude larger, but also opposite in phase. Therefore, the oscillations in $\kappa_{\parallel}(B)$ are antiphase with the quantum oscillating electronic DOS of a Weyl pocket. However, the huge MQOs of $\kappa_{\parallel}(B)$ are hardly observed in $\kappa_{\perp}(B)$ (Fig. 9c). Meanwhile, background thermal conductivity $\kappa_{bg}(B)$ can be enhanced by the parallel B, and this smooth increase can support the notion of exotic heat carriers which tend to carry an increasing amount of heat with an increasing B. Thus, giant MQOs in $\kappa_{\parallel}(B)$ can be attributed to the presence of CZS in Weyl fermions. On the one hand, for $\kappa_{\parallel}(B)$, strong MQOs can be caused by the inverse relationship between CZS velocity and electronic DOS at the Fermi level, and enhancement of $\kappa_{bg}(B)$ can be attributed to the positive connection between CZS velocity and B. On the other hand, the weak response of $\kappa_{\perp}(B)$ can be explained by the small contribution of CZS to C under the perpendicular B. Moreover, the consistency of calculation and experimental results further verifies that CZS is the dominant mechanism of giant MQOs.

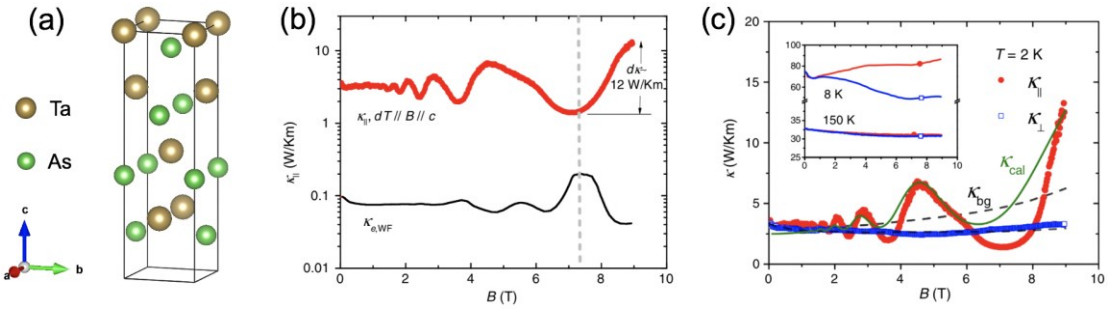

Figure. 9: *(a) Crystal structure of TaAs. (b) B dependence of measured $\kappa_{\parallel}$ ($dT \parallel B \parallel$ c-axis) and $\kappa_{e,WF}$ calculated based on the WF law. (c) B dependence of $\kappa_{\parallel}$, $\kappa_{\perp}$ ($dT \parallel$ c-axis, $B \parallel$ a-axis), κ_{bg} and κ_{cal}. κ_{cal} is calculated based on the CZS scenario. Fig. 9b and 9c reproduced with permission from Xiang, J. et al., Phys. Rev. X, 9, 031036 2019;*[175] *licensed under a Creative Commons Attribution (CC BY) license.*

D. Thermal characterization as probe of coupling between heat carriers

The coupling between spin excitations and phonons plays an important role in magnetic thermal transport[176] and the spin Seebeck effect[177]. Thermal property measurements provide a unique probe of the fundamental transport length scales and coupling mechanisms of spin excitations. Recently, Chen *et al.* combined the first-principles calculations with C and κ measurements to study the spinon-phonon coupling in the 1D $S-1/2$ Heisenberg spin chain compound Ca_2CuO_3 (Fig. 10a).[50] κ_{spin} can be obtained by subtracting the calculated κ_{ph} from the measured κ_{tot}. Fig. 10b shows the extracted κ_{spin}, which peaks at about 90 K and decreases with increasing T. Based on the kinetic model of 1D spinon thermal transport, which was constructed by considering defect and phonon scattering of spinons, the T-dependent spinon MFP (Fig. 10c) was derived from κ_{spin}. It has been found that defect scattering is the leading mechanism below 50 K, while optical phonon scattering is dominant at higher T. Moreover, the obtained spinon-phonon coupling constant is found to be smaller than 0.2, which is consistent with theoretical calculations,[85,178] indicating weak spinon-phonon coupling in these 1D cuprates.

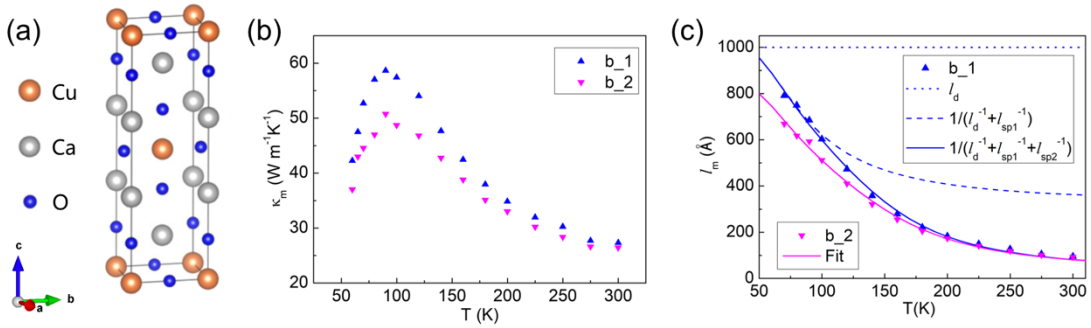

Figure. 10*: (a) Crystal structure of Ca_2CuO_3. (b) κ_{spin} of Ca_2CuO_3 along the spin chain axis. (c) Calculated spinon MFP. l_d and l_{sp} represent the MFPs due to spinon-defect and spinon-phonon scatterings, respectively. Fig. 10b and 10c reproduced with permission from Phys. Rev. Lett. 122, 185901 (2019).*[50] *Copyright 2019 American Physical Society.*

Nanoscale thermal transport methods also play an important role in the probing the coupling between heat carriers. For example, TDTR is a well-established pump-probe technique for thermal transport measurements,[179,180] which are sensitive to the magnon-phonon temperature equilibrium length scale. Hohensee *et al.* determined an effective volumetric magnon-phonon coupling for the two-leg spin ladder cuprate $Ca_9La_5Cu_{24}O_{41}$ using TDTR.[181] It has been found that the coupling constant varies by about two orders of magnitude over T range of 70-300 K.

Lee *et al.* measured the κ of metallic VO_2 nanobeams by the suspended micro-bridge method.[182] VO_2 exhibits a metal-insulator transition (MIT) at 340 K, as shown in Fig. 11a and b. A large violation of the WF law near its MIT was observed. As shown in Fig. 11c, κ_e^0 estimated from the WF law jumps greater than the measured κ_{tot} in the vicinity of MIT. This abnormal behavior leads to negative κ_{ph} and a breakdown of the WF law. To better understand this anomaly, the authors calculated κ_{ph} in two phases using a first-principles method (Fig. 11d). The effective Lorenz number L_{eff} calculated from the difference between κ_{tot} and κ_{ph}^M in the M phase is

found to be $0.11L_0$, which is almost an order of magnitude lower than the Sommerfeld value. Such unusually low κ_e values in the M phase were considered as evidence of the absence of quasi-particles in a strongly correlated electron fluid where heat and charge diffuse independently.

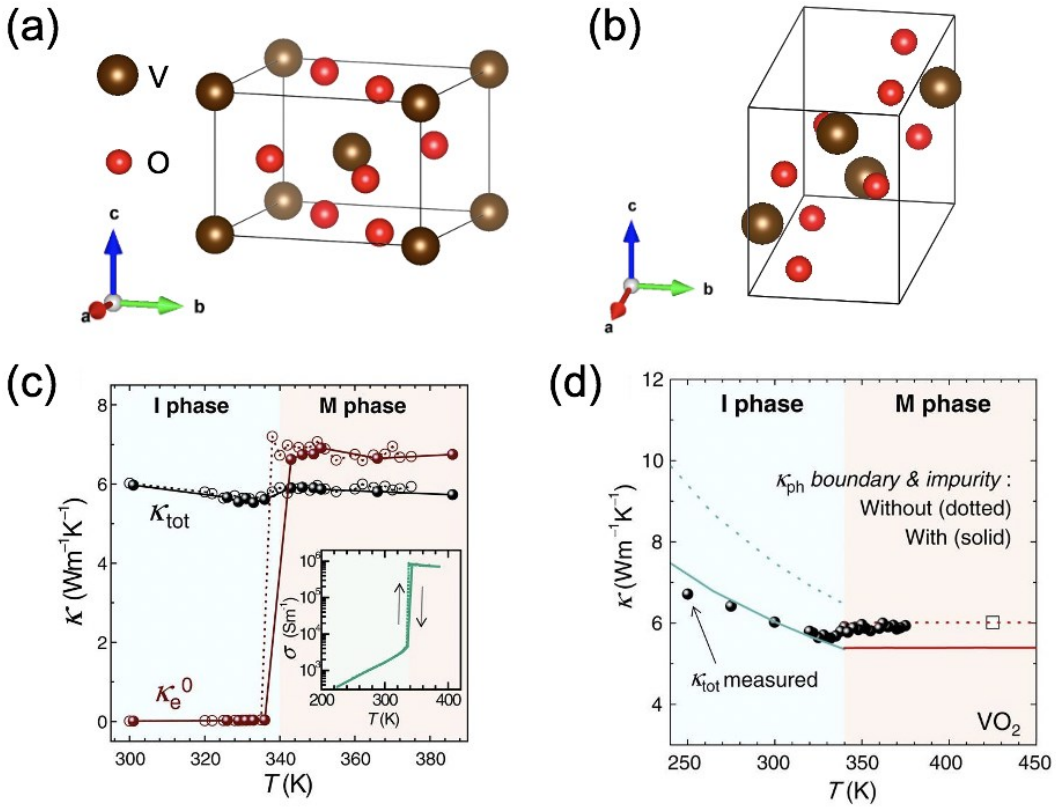

***Figure. 11**: (a) Crystal structure of VO_2 (I phase). (b) Crystal structure of VO_2 (M phase). (c) T dependence of measured κ_{tot} and expected electronic thermal conductivity ($\kappa_e^0 = L_0\sigma T$) of a VO_2 nano-beam. Inset: T dependence of measured σ. (d) Calculated phonon thermal conductivity in the I (κ_{ph}^I) and M (κ_{ph}^M) phases. Fig.11b and 11c reproduced with permission from Science. 355, 371–374 (2017).[182] Copyright 2017 American Association for the Advancement of Science.*

Furthermore, in charge density wave (CDW) materials, thermal transport measurements can reveal the coupling between electrons and phonons, which can make κ no longer follow the conventional T dependence, but instead behave anomalously. Yang *et al*. studied the thermal transport in niobium triselenide ($NbSe_3$) nanowires with a quasi-1D crystal structure. Between two CDW transition temperatures, the T dependence of κ_{ph} exhibits an unusual concave-down curve, while κ_e shows an opposite trend.[183] This phenomenon was attributed to the strong electron-phonon scattering during the CDW phase transitions. Additionally, in tantalum disulfide (1T-TaS_2), the strong electron-phonon scattering arising from the nested Fermi surface interplaying with unique phonon dispersions leads to a T-independent κ_{ph}.[184]

E. Thermal characterization as probe of quantum phase transitions

The physical properties of quantum materials can be attributed to the formation of unique

quantum phases. Therefore, it is crucial to identify the quantum phases and detect phase transitions in quantum materials. For example, THE measurements can be used to study the pseudogap phase of hole-doped cuprates (Fig. 12a). Compared with other unconventional superconductors whose superconductivity and magnetism are intimately related,[185] hole-doped cuprates are classified as a unique category because the original magnetism is replaced by the pseudogap phase, which only appears below the critical hole doping value (p^*).[186] The pseudogap phase is described by a long-range order phase where two electron-current loops with opposite magnetic moments flow in one unit cell.[187] While it was first characterized by photoemission technique[188] and polarized neutron scattering,[189,190] there is no abrupt change of C and electronic properties in this phase transition.[191] Grissonnanche *et al*. reported that a relatively large negative κ_{xy} is a signature of the pseudogap phase in hole-doped $Nd_xLa_{2-x}CuO_4$ and $Eu_xLa_{2-x}CuO_4$ (Fig. 12b).[192] As shown in Fig. 12c, the κ_{xy} values of the samples with doping level (p) below p^* of ~0.2 are negative at low T. Meanwhile, the κ_{xy} of pure La_2CuO_4 is negative across the entire T range, which can be considered a signature for undoped *Mott* insulators. Fig. 12d shows that κ_{xy} becomes positive for the samples with $p \geq p^*$. This finding further confirms that the negative κ_{xy} is a signature for the pseudogap phase. Since mobile charge carriers and magnons are unlikely to cause the observed κ_{xy}, the negative thermal Hall response is likely to be generated by chiral phonons inside the pseudogap phase.[193]

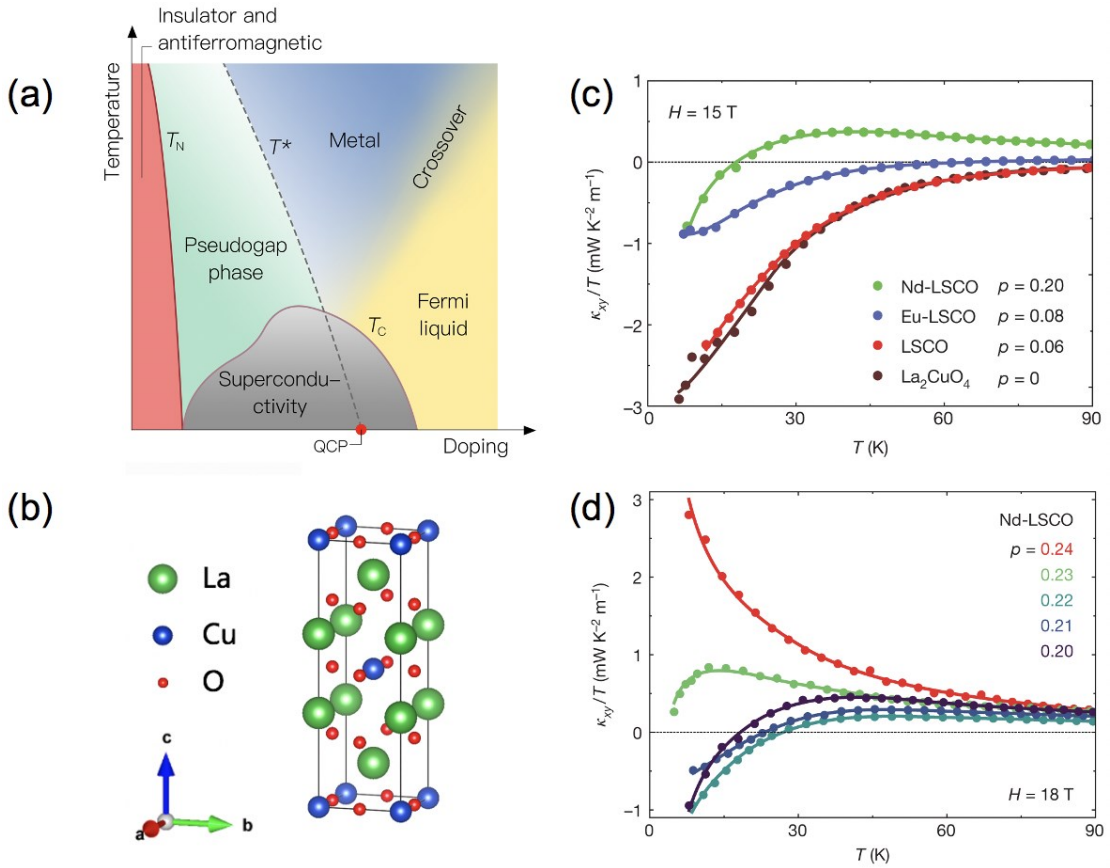

Figure. 12: *(a) Phase diagram of cuprate superconductors. (b) Crystal structure of La_2CuO_4. (c) T dependence of κ_{xy}/T for Mott insulator La_2CuO_4 and three doped samples where $p < p^*$. Nd-LSCO ($La_{1.6-x}Nd_{0.4}Sr_xCuO_4$) and Eu-LSCO ($La_{1.8-x}Eu_{0.2}Sr_xCuO_4$)[194,195] have a p^* of 0.23, and LSCO ($La_{2-x}Sr_xCuO_4$)[196] has a p^* of ~0.18. (d) T dependence of κ_{xy}/T across p^* for Nd-doped samples. Fig. 12c and 12d reproduced with permission from Nature*

571, 376–380 (2019).[192] *Copyright 2019 Springer Nature.*

Thermal characterization can also be used to detect spin-phase transitions in quantum materials. The helimagnetic insulator Cu_2OSeO_3[197] compound exhibits five spin phases at low T, including the helical, conical, tilted conical (TC) and low-T skyrmion (LTS) as well as fully polarized phases. Among them, the TC and LTS phases were once discovered by small-angle neutron scattering measurements[198,199] and more recently probed through κ measurements under external B, where the magnitude of κ changes abruptly across different spin phases.[197]

F. Thermal characterization as probe of quasi-particle hydrodynamics

In non-metallic solids, phonon transport is mainly influenced by three types of scattering processes: diffuse boundary scattering (B-scattering), normal phonon-phonon scattering (N-scattering) and *R*-scattering (combination of Umklapp- and impurity-scattering).[200,201] By comparing the τ of the above scattering processes, three regimes of phonon transport can be divided by the dominant scattering mechanism: ballistic ($\tau_B \ll \tau_R$, τ_N), hydrodynamic ($\tau_N \ll \tau_B \ll \tau_R$) and diffusive regimes ($\tau_R \ll \tau_B$). Hydrodynamic phonon transport can lead to novel T and size dependence of κ and open up the possibility of achieving ultrahigh-κ materials for thermal transport.[202] To observe hydrodynamic transport, which is dominated by N-scattering, both large anharmonicity and high Debye temperature are required. Possible evidence of hydrodynamic phonon transport has been observed in graphite[48] and $SrTiO_3$[203].

Machida *et al*. investigated hydrodynamic phonon transport in thin graphite with combined κ and C measurements.[48] Below 10 K, the slope of κ is close to that of C (Fig. 13a), following the $T^{2.5}$ dependence.[204] The 2.5 exponent is caused by a combination of T^3 and T^2 contributions by *out-of-plane* and *in-plane* phonons.[205] In the *T* range between 10 and 20 K, the higher evolution rate of κ greater than $T^{2.5}$ suggests the existence of hydrodynamic phonon fluid. This difference is much easier to recognize in Fig. 13b. A comparison with $C/T^{2.5}$ and $\kappa/T^{2.5}$ shows a significant maximum above 10 K. Further evidence is the nonmonotonic T dependence of thermal diffusivity (D_{th}) between 10 and 20 K (Fig. 13c), which can be attributed to increased N-scattering. Aside from the unusual T dependence of κ, second sound, which is wavelike thermal transport, has been observed in graphite by using time-resolved optical measurement.[206,207] The experimental data are in good agreement with the *ab initio* calculations predicting wavelike phonon hydrodynamics, as shown in Fig. 13d.

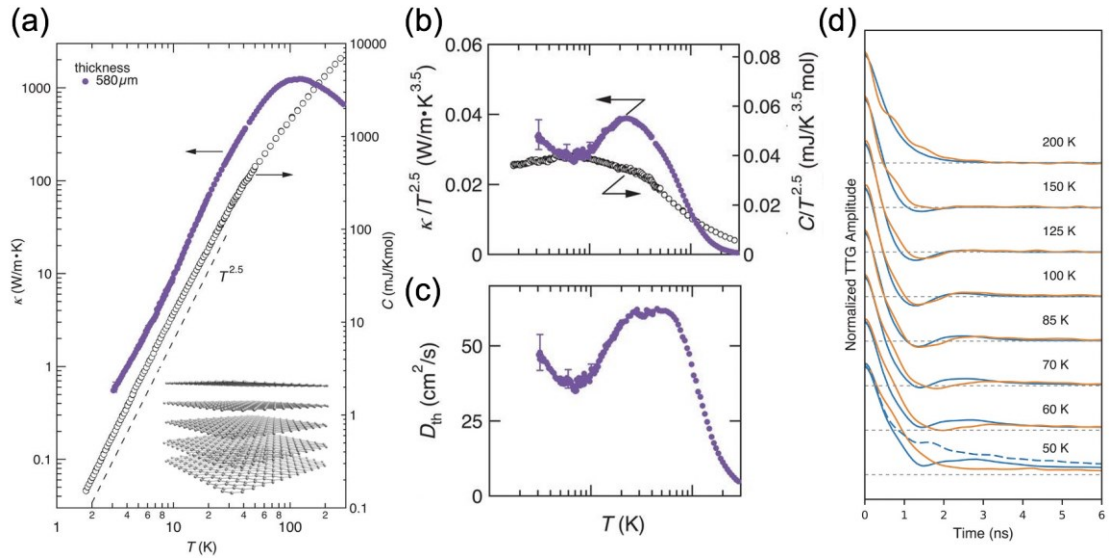

Figure. 13: *(a) T dependence of C and in-plane κ of a 580-nm-thick graphite sample. Inset: Side view of the crystal structure of graphite. (b) T-dependent $\kappa/T^{2.5}$ and $C/T^{2.5}$. (c) T dependence of D_{th}. (d) T dependence of transient thermal grating (TTG) dynamics for graphite. Orange curves: Measured TTG signals. Blue solid curves: simulated responses. Horizontal dashed lines: zero for each pair of curves. Blue dashed curve at 50 K: calculated response in the ballistic limit. Fig. 13a, 13b and 13c reproduced with permission from Science. 367, 309–312 (2020).*[48] *Copyright 2020 American Association for the Advancement of Science. Fig. 13d reproduced with permission from Science. 364, 375–379 (2019).*[206] *Copyright 2019, American Association for the Advancement of Science.*

In addition to phonon hydrodynamics, experimental signatures of hydrodynamic electron flow were also observed in the Weyl semimetal WP_2 by Gooth *et al.*[208] Through thermal and magnetoelectric measurements, the dependence of σ on the sample width and the strong violation of Wiedemann-Franz law prove the existence of hydrodynamic electron fluid below 20 K. Furthermore, Prasai *et al*. discovered a large magnon contribution to κ in the helimagnetic insulator Cu_2OSeO_3.[47] The obtained magnon MFP significantly exceeds the specimen size at low T, suggesting possible Poiseuille flow of magnons.[209–211]

IV. SUMMARY AND OUTLOOK

In this review, the unique role of thermal characterization in investigating emerging quantum materials is discussed. Compared with electrical measurements, thermal characterization can provide the useful information about the exotic physical properties of electrical insulators, such as TIs and QSLs. Charge-neutral spin excitations which are difficult to probe electrically, can be detected with thermal characterization. Thermal characterization can be used to probe the QSLs, Berry curvature, chiral anomaly, coupling between heat carriers, quantum phase transitions, and quasi-particle hydrodynamics in various quantum materials. These new findings lead to a better understanding of exotic physical properties in quantum materials, which can enable the development of novel applications based on quantum materials, such as energy conversion, quantum computing and quantum information processing.

The development of novel characterization techniques has the capacity to enhance the capability of thermal measurements. SThM, a novel approach to study local thermal information by controlling and monitoring the probe–sample heat exchange processes, is a useful probe for characterizing the thermal properties of materials at the nano, atomic and even quantum scales.[63] For example, picowatt-resolution probe of SThM can be used to detect thermal transport at single-metal-atom and single-molecule junctions.[212,213] This measurement is of great fundamental interest due to the distinctive quantum effects expected to arise in atomic structures. As for the thermal properties of nanostructures, an evolved four-probe suspended measurement method[214] has been reported recently. This novel method exploits the variation in heat flow along the suspended nanostructure and across its contacts to four suspended heater and thermometer lines, which can obtain the intrinsic κ of nanostructures and eliminate the contact thermal resistance errors. In addition, micro-Brillouin light scattering, which was designed to characterize the local T of low-frequency acoustic phonons with sub-micron spatial resolution, can detect local non-equilibrium between different energy carriers through combining with micro-Raman spectroscopy and infrared spectroscopy.[215–219] Combining thermal characterization with optical measurements can provide a more complete picture of thermal transport mechanisms. It is expected that novel quantum properties can be discovered with the development of these new characterization techniques.

Despite remarkable progress in research, several physical properties of quantum materials remain to be explored through thermal characterization. One example of this is TIs, in which the existence of topological Andreev bound states in a Josephson junction is expected to result in phase-dependent κ.[220] Experimental realization of this prediction can lead to the development of phase-coherent caloritronic devices.[221] Furthermore, the effect of interlayer rotation on thermal transport in van der Waals bilayer systems has been investigated theoretically. Both in-plane and out-plane thermal transport can be significantly affected by rotation angle.[222,223] A recent experimental work has reported extremely anisotropic thermal transport in MoS_2/WS_2 thin films with random interlayer rotations.[224] It should also be noted that striking quantum states can be achieved in Moiré systems.[225] It would be interesting to study the novel thermal transport properties of these quantum states. As for QSLs, Nasu *et al*. investigated the thermal transport originating from the emergent fractional quasi-particles in KSL by using quantum Monte Carlo simulations.[226] They provided the first quantitative theory for thermal transport, which is a useful tool for probing the QSL signal in Kitaev candidate materials. In addition, the mechanisms behind the THE are not well understood. For example, it has been predicted that magnons and phonons can hybridize into magnetoelastic excitations such that the THE arises from the highly entangled motion of the lattice and spin degrees of freedom.[227,228] These predictions need to be further verified by carefully designed thermal measurements.

ACKNOWLEDGMENTS

We acknowledge support from the National Science Foundation under Grant No. 2144328.

AUTHOR DECLARATIONS

Conflicts of interest

The authors have no conflicts to disclose.

DATA AVAILABILITY

The data that support the findings of this study are available within the article.

Reference

1. The rise of quantum materials. *Nat. Phys.* **12**, 105–105 (2016).
2. Han, W., Maekawa, S. & Xie, X.-C. Spin current as a probe of quantum materials. *Nat. Mater.* **19**, 139–152 (2020).
3. Anderson, P. W. *The Theory of Superconductivity in the High-Tc Cuprates*. (Princeton University Press, 1997).
4. Schrieffer, J. R. *Theory of Superconductivity*. (CRC Press, 2018).
5. Orenstein, J. & Millis, A. J. Advances in the Physics of High-Temperature Superconductivity. *Science.* **288**, 468–474 (2000).
6. Damascelli, A., Hussain, Z. & Shen, Z.-X. Angle-resolved photoemission studies of the cuprate superconductors. *Rev. Mod. Phys.* **75**, 473–541 (2003).
7. Lee, P. A., Nagaosa, N. & Wen, X.-G. Doping a Mott insulator: Physics of high-temperature superconductivity. *Rev. Mod. Phys.* **78**, 17–85 (2006).
8. Hasan, M. Z. & Kane, C. L. Colloquium : Topological insulators. *Rev. Mod. Phys.* **82**, 3045–3067 (2010).
9. Qi, X.-L. & Zhang, S.-C. Topological insulators and superconductors. *Rev. Mod. Phys.* **83**, 1057–1110 (2011).
10. Wang, J. & Zhang, S.-C. Topological states of condensed matter. *Nat. Mater.* **16**, 1062–1067 (2017).
11. Burkov, A. A. Topological semimetals. *Nat. Mater.* **15**, 1145–1148 (2016).
12. Manna, K., Sun, Y., Muechler, L., Kübler, J. & Felser, C. Heusler, Weyl and Berry. *Nat. Rev. Mater.* **3**, 244–256 (2018).
13. Neupane, M. *et al.* Observation of a three-dimensional topological Dirac semimetal phase in high-mobility Cd_3As_2. *Nat. Commun.* **5**, 3786 (2014).
14. Huang, S.-M. *et al.* A Weyl Fermion semimetal with surface Fermi arcs in the transition metal monopnictide TaAs class. *Nat. Commun.* **6**, 7373 (2015).
15. Xu, S.-Y. *et al.* Discovery of a Weyl fermion semimetal and topological Fermi arcs. *Science.* **349**, 613–617 (2015).
16. Xu, S.-Y. *et al.* Observation of Fermi arc surface states in a topological metal. *Science.* **347**, 294–298 (2015).
17. Savary, L. & Balents, L. Quantum spin liquids: a review. *Reports Prog. Phys.* **80**, 016502 (2017).
18. Meng, Z. Y., Lang, T. C., Wessel, S., Assaad, F. F. & Muramatsu, A. Quantum spin liquid emerging in two-dimensional correlated Dirac fermions. *Nature* **464**, 847–851 (2010).
19. Broholm, C. *et al.* Quantum spin liquids. *Science.* **367**, (2020).
20. Sonin, E. B. Spin currents and spin superfluidity. *Adv. Phys.* **59**, 181–255 (2010).
21. Bonaccorso, F., Sun, Z., Hasan, T. & Ferrari, A. C. Graphene photonics and optoelectronics.

Nat. Photonics **4**, 611–622 (2010).
22. Beenakker, C. W. J. Colloquium : Andreev reflection and Klein tunneling in graphene. *Rev. Mod. Phys.* **80**, 1337–1354 (2008).
23. GEIM, A. K. & NOVOSELOV, K. S. The rise of graphene. in *Nanoscience and Technology* 11–19 (Co-Published with Macmillan Publishers Ltd, UK, 2009).
24. Novoselov, K. S. *et al.* Two-dimensional gas of massless Dirac fermions in graphene. *Nature* **438**, 197–200 (2005).
25. Kane, C. L. & Mele, E. J. Quantum Spin Hall Effect in Graphene. *Phys. Rev. Lett.* **95**, 226801 (2005).
26. Wang, Q. H., Kalantar-Zadeh, K., Kis, A., Coleman, J. N. & Strano, M. S. Electronics and optoelectronics of two-dimensional transition metal dichalcogenides. *Nat. Nanotechnol.* **7**, 699–712 (2012).
27. Mak, K. F. & Shan, J. Photonics and optoelectronics of 2D semiconductor transition metal dichalcogenides. *Nat. Photonics* **10**, 216–226 (2016).
28. Andrei, E. Y. *et al.* The marvels of moiré materials. *Nat. Rev. Mater.* **6**, 201–206 (2021).
29. Thomas, H. *et al.* Superconducting transmission lines – Sustainable electric energy transfer with higher public acceptance? *Renew. Sustain. Energy Rev.* **55**, 59–72 (2016).
30. Yin, J. *et al.* Indium- and Platinum-Free Counter Electrode for Green Mesoscopic Photovoltaics through Graphene Electrode and Graphene Composite Catalysts: Interfacial Compatibility. *ACS Appl. Mater. Interfaces* **8**, 5314–5319 (2016).
31. Das, S., Pandey, D., Thomas, J. & Roy, T. The Role of Graphene and Other 2D Materials in Solar Photovoltaics. *Adv. Mater.* **31**, 1802722 (2019).
32. König, M. *et al.* Quantum Spin Hall Insulator State in HgTe Quantum Wells. *Science.* **318**, 766–770 (2007).
33. Yue, Z., Cai, B., Wang, L., Wang, X. & Gu, M. Intrinsically core-shell plasmonic dielectric nanostructures with ultrahigh refractive index. *Sci. Adv.* **2**, (2016).
34. Yue, Z., Xue, G., Liu, J., Wang, Y. & Gu, M. Nanometric holograms based on a topological insulator material. *Nat. Commun.* **8**, 15354 (2017).
35. Armitage, N. P., Mele, E. J. & Vishwanath, A. Weyl and Dirac semimetals in three-dimensional solids. *Rev. Mod. Phys.* **90**, 015001 (2018).
36. Alicea, J., Oreg, Y., Refael, G., von Oppen, F. & Fisher, M. P. A. Non-Abelian statistics and topological quantum information processing in 1D wire networks. *Nat. Phys.* **7**, 412–417 (2011).
37. Wang, H. *et al.* Observation of superconductivity induced by a point contact on 3D Dirac semimetal Cd_3As_2 crystals. *Nat. Mater.* **15**, 38–42 (2016).
38. Gooth, J., Schierning, G., Felser, C. & Nielsch, K. Quantum materials for thermoelectricity. *MRS Bull.* **43**, 187–192 (2018).
39. Liu, X. & Hersam, M. C. 2D materials for quantum information science. *Nat. Rev. Mater.* **4**, 669–684 (2019).
40. Eckstein, J. N. & Levy, J. Materials issues for quantum computation. *MRS Bull.* **38**, 783–789 (2013).
41. Fontes, A. *et al.* Quantum Dots in Biomedical Research. in *Biomedical Engineering - Technical Applications in Medicine* (InTech, 2012).
42. *Ionizing Radiation Effects and Applications*. (InTech, 2018).

43. Abbasi, E. *et al.* Biomedical and biological applications of quantum dots. *Artif. Cells, Nanomedicine, Biotechnol.* 1–7 (2015)
44. Li, M. & Chen, G. Thermal transport for probing quantum materials. *MRS Bull.* **45**, 348–356 (2020).
45. Guo, S., Xu, Y., Cheng, R., Zhou, J. & Chen, X. Thermal Hall effect in insulating quantum materials. *Innov.* **3**, 100290 (2022).
46. Burger, N. *et al.* Review of thermal conductivity in composites: Mechanisms, parameters and theory. *Prog. Polym. Sci.* **61**, 1–28 (2016).
47. Prasai, N. *et al.* Ballistic magnon heat conduction and possible Poiseuille flow in the helimagnetic insulator Cu_2OSeO_3. *Phys. Rev. B* **95**, 224407 (2017).
48. Machida, Y., Matsumoto, N., Isono, T. & Behnia, K. Phonon hydrodynamics and ultrahigh–room-temperature thermal conductivity in thin graphite. *Science.* **367**, 309–312 (2020).
49. Li, S., Guo, S., Xu, Y., Zhou, J. & Chen, X. Role of Grain Size on Magnon and Phonon Thermal Transport in the Spin Ladder Compound $Ca_9La_5Cu_{24}O_{41}$. *ACS Appl. Electron. Mater.* **4**, 787–794 (2022).
50. Chen, X. *et al.* Coupling of Spinons with Defects and Phonons in the Spin Chain Compound Ca_2CuO_3 *Phys. Rev. Lett.* **122**, 185901 (2019).
51. Hess, C. *et al.* Magnon Heat Transport in Doped La_2CuO_4. *Phys. Rev. Lett.* **90**, 197002 (2003).
52. Balents, L. Spin liquids in frustrated magnets. *Nature* **464**, 199–208 (2010).
53. Zhou, Y., Kanoda, K. & Ng, T.-K. Quantum spin liquid states. *Rev. Mod. Phys.* **89**, 025003 (2017).
54. Kasahara, Y. *et al.* Majorana quantization and half-integer thermal quantum Hall effect in a Kitaev spin liquid. *Nature* **559**, 227–231 (2018).
55. Nasu, J., Udagawa, M. & Motome, Y. Thermal fractionalization of quantum spins in a Kitaev model: Temperature-linear specific heat and coherent transport of Majorana fermions. *Phys. Rev. B* **92**, 115122 (2015).
56. Wang, Z., Qi, X.-L. & Zhang, S.-C. Topological field theory and thermal responses of interacting topological superconductors. *Phys. Rev. B* **84**, 014527 (2011).
57. Noky, J., Gooth, J., Felser, C. & Sun, Y. Characterization of topological band structures away from the Fermi level by the anomalous Nernst effect. *Phys. Rev. B* **98**, 241106 (2018).
58. Hartnoll, S. A., Kovtun, P. K., Müller, M. & Sachdev, S. Theory of the Nernst effect near quantum phase transitions in condensed matter and in dyonic black holes. *Phys. Rev. B* **76**, 144502 (2007).
59. Xu, Y., Zhou, X. & Jin, G. Detecting topological phases in silicene by anomalous Nernst effect. *Appl. Phys. Lett.* **108**, 203104 (2016).
60. Cheng, R., Okamoto, S. & Xiao, D. Spin Nernst Effect of Magnons in Collinear Antiferromagnets. *Phys. Rev. Lett.* **117**, 217202 (2016).
61. Yang, H. *et al.* Giant anomalous Nernst effect in the magnetic Weyl $Co_3Sn_2S_2$. *Phys. Rev. Mater.* **4**, 024202 (2020).
62. Gomès, S., Assy, A. & Chapuis, P.-O. Scanning thermal microscopy: A review. *Phys. status solidi* **212**, 477–494 (2015).
63. Zhang, Y. *et al.* A Review on Principles and Applications of Scanning Thermal Microscopy (SThM). *Adv. Funct. Mater.* **30**, 1900892 (2020).
64. Schwabl, F. *Quantum Mechanics*. (Springer Berlin Heidelberg, 2007).

65. Howard, E. Modern condensed matter physics. *Contemp. Phys.* **60**, 268–268 (2019).
66. Debye, P. Zur Theorie der spezifischen Wärmen. *Ann. Phys.* **344**, 789–839 (1912).
67. Petit, A. T. & Dulong, P. L. Recherches sur Quelques Points Importants de la Théorie de la Chaleur, Annales de Chimie et de Physique 10, 395-413 (1819).
68. Yu, P. Y. & Cardona, M. *Fundamentals of Semiconductors*. (Springer Berlin Heidelberg, 2010).
69. Berman, R., Foster, E. L. & Ziman, J. M. Thermal conduction in artificial sapphire crystals at low temperatures I. Nearly perfect crystals. *Proc. R. Soc. London. Ser. A. Math. Phys. Sci.* **231**, 130–144 (1955).
70. Aksamija, Z. & Knezevic, I. Lattice thermal conductivity of graphene nanoribbons: Anisotropy and edge roughness scattering. *Appl. Phys. Lett.* **98**, 141919 (2011).
71. Evans, W. J., Hu, L. & Keblinski, P. Thermal conductivity of graphene ribbons from equilibrium molecular dynamics: Effect of ribbon width, edge roughness, and hydrogen termination. *Appl. Phys. Lett.* **96**, 203112 (2010).
72. Savin, A. V., Kivshar, Y. S. & Hu, B. Suppression of thermal conductivity in graphene nanoribbons with rough edges. *Phys. Rev. B* **82**, 195422 (2010).
73. Klemens, P. G. The Scattering of Low-Frequency Lattice Waves by Static Imperfections. *Proc. Phys. Soc. Sect. A* **68**, 1113–1128 (1955).
74. Zhou, J. *et al.* Direct observation of large electron–phonon interaction effect on phonon heat transport. *Nat. Commun.* **11**, 6040 (2020).
75. Liao, B. *et al.* Significant Reduction of Lattice Thermal Conductivity by the Electron-Phonon Interaction in Silicon with High Carrier Concentrations: A First-Principles Study. *Phys. Rev. Lett.* **114**, 115901 (2015).
76. Uher, C. Thermal Conductivity of Metals. In: Tritt, T.M. (eds) Thermal Conductivity. *Physics of Solids and Liquids*. (Springer, 2004).
77. Monachon, C., Weber, L. & Dames, C. Thermal Boundary Conductance: A Materials Science Perspective. *Annu. Rev. Mater. Res.* **46**, 433-463 (2016).
78. Crossno, J. *et al.* Observation of the Dirac fluid and the breakdown of the Wiedemann-Franz law in graphene. *Science.* **351**, 1058–1061 (2016).
79. Mason, S. J. *et al.* Violation of the Wiedemann-Franz law through reduction of thermal conductivity in gold thin films. *Phys. Rev. Mater.* **4**, 065003 (2020).
80. Tanatar, M. A., Paglione, J., Petrovic, C. & Taillefer, L. Anisotropic Violation of the Wiedemann-Franz Law at a Quantum Critical Point. *Science.* **316**, 1320–1322 (2007).
81. Hess, C. *et al.* Magnon heat transport in $(Sr,Ca,La)_{14}Cu_{24}O_{41}$. *Phys. Rev. B* **64**, 184305 (2001).
82. Li, Y., Zhao, C., Zhang, W., Hoffmann, A. & Novosad, V. Advances in coherent coupling between magnons and acoustic phonons. *APL Mater.* **9**, 060902 (2021).
83. Stamokostas, G. L., Lapas, P. E. & Fiete, G. A. Thermal conductivity of local moment models with strong spin-orbit coupling. *Phys. Rev. B* **95**, 064410 (2017).
84. Chen, X. *et al.* Effects of grain boundaries and defects on anisotropic magnon transport in textured $Sr_{14}Cu_{24}O_{41}$. *Phys. Rev. B* **95**, 144310 (2017).
85. Chernyshev, A. L. Strong quantum effects in an almost classical antiferromagnet on a kagome lattice. *Phys. Rev. B* **92**, 094409 (2015).
86. Dobin, A. Y. & Victora, R. H. Intrinsic Nonlinear Ferromagnetic Relaxation in Thin Metallic Films. *Phys. Rev. Lett.* **90**, 167203 (2003).

87. Hess, C. *et al.* Magnon-Hole Scattering and Charge Order in $Sr_{14-x}Ca_xCu_{24}O_{41}$. *Phys. Rev. Lett.* **93**, 027005 (2004).
88. Cottam, M. G. Theory of two-magnon Raman scattering in antiferromagnets at finite temperatures. *J. Phys. C Solid State Phys.* **5**, 1461–1474 (1972).
89. Liao, B., Zhou, J. & Chen, G. Generalized Two-Temperature Model for Coupled Phonon-Magnon Diffusion. *Phys. Rev. Lett.* **113**, 025902 (2014).
90. Karbach, M., Hu, K. & Müller, G. Introduction to the Bethe Ansatz II. *Comput. Phys.* **12**, 565 (1998).
91. Karbach, M., Hu, K. & Muller, G. Introduction to the Bethe Ansatz III. (2000).
92. Klümper, A. & Sakai, K. The thermal conductivity of the spin-½ XXZ chain at arbitrary temperature. *J. Phys. A. Math. Gen.* **35**, 2173–2182 (2002).
93. Sologubenko, A. V., Lorenz, T., Ott, H. R. & Freimuth, A. Thermal Conductivity via Magnetic Excitations in Spin-Chain Materials. *J. Low Temp. Phys.* **147**, 387–403 (2007).
94. Shimshoni, E., Andrei, N. & Rosch, A. Thermal conductivity of spin-½ chains. *Phys. Rev. B* **68**, 104401 (2003).
95. Hlubek, N. *et al.* Ballistic heat transport of quantum spin excitations as seen in $SrCuO_2$ *Phys. Rev. B* **81**, 020405 (2010).
96. Takahashi, N. *et al.* Evidence for Ballistic Thermal Conduction in the One-Dimensional Spin System Sr_2CuO_3. in *AIP Conference Proceedings* vol. 850 1265–1266 (AIP, 2006).
97. Hlubek, N. *et al.* Spinon heat transport and spin–phonon interaction in the spin-1/2 Heisenberg chain cuprates Sr_2CuO_3 and $SrCuO_2$. *J. Stat. Mech. Theory Exp.* **2012**, P03006 (2012).
98. IV. On the dynamical theory of gases. *Philos. Trans. R. Soc. London* **157**, 49–88 (1867).
99. Chen, G. Nanoscale energy transport and conversion : a parallel treatment of electrons, molecules, phonons, and photons. in (2005).
100. Blatt, F. J. Matthiessen's rule. (McGraw Hill, New York, 2020).
101. Zhao, D., Qian, X., Gu, X., Jajja, S. A. & Yang, R. Measurement Techniques for Thermal Conductivity and Interfacial Thermal Conductance of Bulk and Thin Film Materials. *J. Electron. Packag.* **138**, (2016).
102. Cahill, D. G. Analysis of heat flow in layered structures for time-domain thermoreflectance. *Rev. Sci. Instrum.* **75**, 5119–5122 (2004).
103. Cahill, D. G. Thermal-conductivity measurement by time-domain thermoreflectance. *MRS Bull.* **43**, 782–789 (2018).
104. Kim, P., Shi, L., Majumdar, A. & McEuen, P. L. Thermal Transport Measurements of Individual Multiwalled Nanotubes. *Phys. Rev. Lett.* **87**, 215502 (2001).
105. Shi, L. *et al.* Measuring Thermal and Thermoelectric Properties of One-Dimensional Nanostructures Using a Microfabricated Device. *J. Heat Transfer* **125**, 881–888 (2003).
106. Balandin, A., Wang, K. L., Kouklin, N. & Bandyopadhyay, S. Raman spectroscopy of electrochemically self-assembled CdS quantum dots. *Appl. Phys. Lett.* **76**, 137–139 (2000).
107. Alim, K. A., Fonoberov, V. A., Shamsa, M. & Balandin, A. A. Micro-Raman investigation of optical phonons in ZnO nanocrystals. *J. Appl. Phys.* **97**, 124313 (2005).
108. Calizo, I., Bejenari, I., Rahman, M., Liu, G. & Balandin, A. A. Ultraviolet Raman microscopy of single and multilayer graphene. *J. Appl. Phys.* **106**, 043509 (2009).
109. Lazarenkova, O. L. & Balandin, A. A. Raman scattering from three-dimensionally regimented quantum dot superlattices. *Superlattices Microstruct.* **33**, 95–101 (2003).

110. Duvigneau, J., Schönherr, H. & Vancso, G. J. Nanoscale Thermal AFM of Polymers: Transient Heat Flow Effects. *ACS Nano* **4**, 6932–6940 (2010).
111. Luo, T. & Chen, G. Nanoscale heat transfer – from computation to experiment. *Phys. Chem. Chem. Phys.* **15**, 3389 (2013).
112. Gmelin, E., Fischer, R. & Stitzinger, R. Sub-micrometer thermal physics – An overview on SThM techniques1Presented at the Twelfth Ulm-Freiberg Conference, Freiberg, Germany, 19–21 March 19971. *Thermochim. Acta* **310**, 1–17 (1998).
113. Zhang, Y., Zhu, W., Han, L. & Borca-Tasciuc, T. Quantitative temperature distribution measurements by non-contact scanning thermal microscopy using Wollaston probes under ambient conditions. *Rev. Sci. Instrum.* **91**, 014901 (2020).
114. Xiao, D., Chang, M.-C. & Niu, Q. Berry phase effects on electronic properties. *Rev. Mod. Phys.* **82**, 1959–2007 (2010).
115. Zhang, L. Berry curvature and various thermal Hall effects. *New J. Phys.* **18**, 103039 (2016).
116. Ikhlas, M. *et al.* Large anomalous Nernst effect at room temperature in a chiral antiferromagnet. *Nat. Phys.* **13**, 1085–1090 (2017).
117. Caglieris, F. *et al.* Anomalous Nernst effect and field-induced Lifshitz transition in the Weyl semimetals TaP and TaAs. *Phys. Rev. B* **98**, 201107 (2018).
118. Watzman, S. J. *et al.* Dirac dispersion generates unusually large Nernst effect in Weyl semimetals. *Phys. Rev. B* **97**, 161404 (2018).
119. Wuttke, C. *et al.* Berry curvature unravelled by the anomalous Nernst effect in Mn_3Ge. *Phys. Rev. B* **100**, 085111 (2019).
120. Xiao, D., Yao, Y., Fang, Z. & Niu, Q. Berry-Phase Effect in Anomalous Thermoelectric Transport. *Phys. Rev. Lett.* **97**, 026603 (2006).
121. de Vries, M. A., Kamenev, K. V., Kockelmann, W. A., Sanchez-Benitez, J. & Harrison, A. Magnetic Ground State of an Experimental S=1/2 Kagome Antiferromagnet. *Phys. Rev. Lett.* **100**, 157205 (2008).
122. Fu, M., Imai, T., Han, T.-H. & Lee, Y. S. Evidence for a gapped spin-liquid ground state in a kagome Heisenberg antiferromagnet. *Science.* **350**, 655–658 (2015).
123. Huang, Y. Y. *et al.* Heat Transport in Herbertsmithite: Can a Quantum Spin Liquid Survive Disorder? *Phys. Rev. Lett.* **127**, 267202 (2021).
124. Yamashita, M. *et al.* Highly Mobile Gapless Excitations in a Two-Dimensional Candidate Quantum Spin Liquid. *Science.* **328**, 1246–1248 (2010).
125. Itou, T., Oyamada, A., Maegawa, S., Tamura, M. & Kato, R. Quantum spin liquid in the spin-1/2 triangular antiferromagnet $EtMe_3Sb[Pd(dmt)_2]_2$. *Phys. Rev. B* **77**, 104413 (2008).
126. Itou, T., Oyamada, A., Maegawa, S. & Kato, R. Instability of a quantum spin liquid in an organic triangular-lattice antiferromagnet. *Nat. Phys.* **6**, 673–676 (2010).
127. Yamashita, S., Yamamoto, T., Nakazawa, Y., Tamura, M. & Kato, R. Gapless spin liquid of an organic triangular compound evidenced by thermodynamic measurements. *Nat. Commun.* **2**, 275 (2011).
128. Watanabe, D. *et al.* Novel Pauli-paramagnetic quantum phase in a Mott insulator. *Nat. Commun.* **3**, 1090 (2012).
129. Bourgeois-Hope, P. *et al.* Thermal Conductivity of the Quantum Spin Liquid Candidate $EtMe_3Sb[Pd(dmt)_2]_2$: No Evidence of Mobile Gapless Excitations. *Phys. Rev. X* **9**, 041051 (2019).

130. Ni, J. M. *et al.* Absence of Magnetic Thermal Conductivity in the Quantum Spin Liquid Candidate $EtMe_3Sb[Pd(dmt)_2]_2$. *Phys. Rev. Lett.* **123**, 247204 (2019).
131. Yamashita, M. *et al.* Presence and absence of itinerant gapless excitations in the quantum spin liquid candidate $EtMe_3Sb[Pd(dmt)_2]_2$. *Phys. Rev. B* **101**, 140407 (2020).
132. Yamashita, S. *et al.* Thermodynamic properties of a spin-1/2 spin-liquid state in a κ-type organic salt. *Nat. Phys.* **4**, 459–462 (2008).
133. Yamashita, M. Boundary-limited and Glassy-like Phonon Thermal Conduction in $EtMe_3Sb[Pd(dmit)_2]_2$. *J. Phys. Soc. Japan* **88**, 083702 (2019).
134. Kitaev, A. Anyons in an exactly solved model and beyond. *Ann. Phys. (N. Y).* **321**, 2–111 (2006).
135. Banerjee, A. *et al.* Proximate Kitaev quantum spin liquid behaviour in a honeycomb magnet. *Nat. Mater.* **15**, 733–740 (2016).
136. Sandilands, L. J., Tian, Y., Plumb, K. W., Kim, Y.-J. & Burch, K. S. Scattering Continuum and Possible Fractionalized Excitations in α−$RuCl_3$. *Phys. Rev. Lett.* **114**, 147201 (2015).
137. Nasu, J., Knolle, J., Kovrizhin, D. L., Motome, Y. & Moessner, R. Fermionic response from fractionalization in an insulating two-dimensional magnet. *Nat. Phys.* **12**, 912–915 (2016).
138. Yokoi, T. *et al.* Half-integer quantized anomalous thermal Hall effect in the Kitaev material candidate α-$RuCl_3$. *Science.* **373**, 568–572 (2021).
139. Czajka, P. *et al.* Oscillations of the thermal conductivity in the spin-liquid state of α-$RuCl_3$. *Nat. Phys.* **17**, 915–919 (2021).
140. Ye, M., Halász, G. B., Savary, L. & Balents, L. Quantization of the Thermal Hall Conductivity at Small Hall Angles. *Phys. Rev. Lett.* **121**, 147201 (2018).
141. Banerjee, M. *et al.* Observed quantization of anyonic heat flow. *Nature* **545**, 75–79 (2017).
142. Suetsugu, S. *et al.* Evidence for the first-order topological phase transition in a Kitaev spin liquid candidate α-$RuCl_3$. (2022).
143. Motrunich, O. I. Orbital magnetic field effects in spin liquid with spinon Fermi sea: Possible application to κ−$(ET)_2Cu_2(CN)_3$. *Phys. Rev. B* **73**, 155115 (2006).
144. Bruin, J. A. N. *et al*. Origin of oscillatory structures in the magnetothermal conductivity of the putative Kitaev magnet α-$RuCl_3$. *APL Mater*. 10, 090703 (2022).
145. Hentrich, R. *et al.* Unusual Phonon Heat Transport in α-$RuCl_3$: Strong Spin-Phonon Scattering and Field-Induced Spin Gap. *Phys. Rev. Lett.* **120**, 117204 (2018).
146. Lefrançois, É. *et al.* Evidence of a Phonon Hall Effect in the Kitaev Spin Liquid Candidate α-$RuCl_3$. *Phys. Rev. X* **12**, 021025 (2022).
147. Yamaji, Y. *et al.* Clues and criteria for designing a Kitaev spin liquid revealed by thermal and spin excitations of the honeycomb iridate Na_2IrO_3. *Phys. Rev. B* **93**, 174425 (2016).
148. Yoshitake, J., Nasu, J. & Motome, Y. Fractional Spin Fluctuations as a Precursor of Quantum Spin Liquids: Majorana Dynamical Mean-Field Study for the Kitaev Model. *Phys. Rev. Lett.* **117**, 157203 (2016).
149. Nasu, J., Udagawa, M. & Motome, Y. Vaporization of Kitaev Spin Liquids. *Phys. Rev. Lett.* **113**, 197205 (2014).
150. Wang, Z. *et al.* Magnetic Excitations and Continuum of a Possibly Field-Induced Quantum Spin Liquid in α-$RuCl_3$. *Phys. Rev. Lett.* **119**, 227202 (2017).
151. Glamazda, A., Lemmens, P., Do, S.-H., Kwon, Y. S. & Choi, K.-Y. Relation between Kitaev magnetism and structure in α-$RuCl_3$. *Phys. Rev. B* **95**, 174429 (2017).

152. Widmann, S. *et al.* Thermodynamic evidence of fractionalized excitations in α-$RuCl_3$. *Phys. Rev. B* **99**, 094415 (2019).
153. Ran, K. *et al.* Spin-Wave Excitations Evidencing the Kitaev Interaction in Single Crystalline α-$RuCl_3$. *Phys. Rev. Lett.* **118**, 107203 (2017).
154. Tanaka, O. *et al.* Thermodynamic evidence for a field-angle-dependent Majorana gap in a Kitaev spin liquid. *Nat. Phys.* **18**, 429–435 (2022).
155. Katsura, H., Nagaosa, N. & Lee, P. A. Theory of the Thermal Hall Effect in Quantum Magnets. *Phys. Rev. Lett.* **104**, 066403 (2010).
156. Xiao, D., Shi, J. & Niu, Q. Berry Phase Correction to Electron Density of States in Solids. *Phys. Rev. Lett.* **95**, 137204 (2005).
157. Nagaosa, N., Sinova, J., Onoda, S., MacDonald, A. H. & Ong, N. P. Anomalous Hall effect. *Rev. Mod. Phys.* **82**, 1539–1592 (2010).
158. Matsumoto, R. & Murakami, S. Theoretical Prediction of a Rotating Magnon Wave Packet in Ferromagnets. *Phys. Rev. Lett.* **106**, 197202 (2011).
159. Matsumoto, R. & Murakami, S. Rotational motion of magnons and the thermal Hall effect. *Phys. Rev. B* **84**, 184406 (2011).
160. Onose, Y. *et al.* Observation of the Magnon Hall Effect. *Science.* **329**, 297–299 (2010).
161. Hirschberger, M., Chisnell, R., Lee, Y. S. & Ong, N. P. Thermal Hall Effect of Spin Excitations in a Kagome Magnet. *Phys. Rev. Lett.* **115**, 106603 (2015).
162. Lee, H., Han, J. H. & Lee, P. A. Thermal Hall effect of spins in a paramagnet. *Phys. Rev. B* **91**, 125413 (2015).
163. Marcipar, L. *et al.* Muon-spin spectroscopy of the organometallic spin-½ kagome-lattice compound Cu(1,3-benzenedicarboxylate). *Phys. Rev. B* **80**, 132402 (2009).
164. Kim, S. Il *et al.* Dense dislocation arrays embedded in grain boundaries for high-performance bulk thermoelectrics. *Science.* **348**, 109–114 (2015).
165. Hirokane, Y., Nii, Y., Tomioka, Y. & Onose, Y. Phononic thermal Hall effect in diluted terbium oxides. *Phys. Rev. B* **99**, 134419 (2019).
166. Wan, X., Turner, A. M., Vishwanath, A. & Savrasov, S. Y. Topological semimetal and Fermi-arc surface states in the electronic structure of pyrochlore iridates. *Phys. Rev. B* **83**, 205101 (2011).
167. Burkov, A. A. & Balents, L. Weyl Semimetal in a Topological Insulator Multilayer. *Phys. Rev. Lett.* **107**, 127205 (2011).
168. Singh, B. *et al.* Topological electronic structure and Weyl semimetal in the $TlBiSe_2$ class of semiconductors. *Phys. Rev. B* **86**, 115208 (2012).
169. Guin, S. N. *et al.* Zero-Field Nernst Effect in a Ferromagnetic Kagome-Lattice Weyl-Semimetal $Co_3Sn_2S_2$. *Adv. Mater.* **31**, 1806622 (2019).
170. Weyl, H. Electron and gravitation. *z. Phys* **56**, 330-352 (1929).
171. Nielsen, H. B. & Ninomiya, M. The Adler-Bell-Jackiw anomaly and Weyl fermions in a crystal. *Phys. Lett. B* **130**, 389–396 (1983).
172. Ong, N. P. & Liang, S. Experimental signatures of the chiral anomaly in Dirac–Weyl semimetals. *Nat. Rev. Phys.* **3**, 394–404 (2021).
173. Spivak, B. Z. & Andreev, A. V. Magnetotransport phenomena related to the chiral anomaly in Weyl semimetals. *Phys. Rev. B* **93**, 085107 (2016).
174. Vu, D. *et al.* Thermal chiral anomaly in the magnetic-field-induced ideal Weyl phase of

$Bi_{1-x}Sb_x$. *Nat. Mater.* **20**, 1525–1531 (2021).
175. Xiang, J. *et al.* Giant Magnetic Quantum Oscillations in the Thermal Conductivity of TaAs: Indications of Chiral Zero Sound. *Phys. Rev. X* **9**, 031036 (2019).
176. Hess, C. Heat transport of cuprate-based low-dimensional quantum magnets with strong exchange coupling. *Phys. Rep.* **811**, 1–38 (2019).
177. Man, H. *et al.* Direct observation of magnon-phonon coupling in yttrium iron garnet. *Phys. Rev. B* **96**, 100406 (2017).
178. Chernyshev, A. L. & Rozhkov, A. V. Heat Transport in Spin Chains with Weak Spin-Phonon Coupling. *Phys. Rev. Lett.* **116**, 017204 (2016).
179. Cahill, D. G. *et al.* Nanoscale thermal transport. *J. Appl. Phys.* **93**, 793–818 (2003).
180. Kang, K., Koh, Y. K., Chiritescu, C., Zheng, X. & Cahill, D. G. Two-tint pump-probe measurements using a femtosecond laser oscillator and sharp-edged optical filters. *Rev. Sci. Instrum.* **79**, 114901 (2008).
181. Hohensee, G. T., Wilson, R. B., Feser, J. P. & Cahill, D. G. Magnon-phonon coupling in the spin-ladder compound $Ca_9La_5Cu_{24}O_{41}$ measured by time-domain thermoreflectance. *Phys. Rev. B* **89**, 024422 (2014).
182. Lee, S. *et al.* Anomalously low electronic thermal conductivity in metallic vanadium dioxide. *Science.* **355**, 371–374 (2017).
183. Yang, L. *et al.* Distinct Signatures of Electron–Phonon Coupling Observed in the Lattice Thermal Conductivity of $NbSe_3$ Nanowires. *Nano Lett.* **19**, 415–421 (2019).
184. Liu, H. *et al.* Anomalously Suppressed Thermal Conduction by Electron-Phonon Coupling in Charge-Density-Wave Tantalum Disulfide. *Adv. Sci.* **7**, 1902071 (2020).
185. Monthoux, P., Pines, D. & Lonzarich, G. G. Superconductivity without phonons. *Nature* **450**, 1177–1183 (2007).
186. Keimer, B., Kivelson, S. A., Norman, M. R., Uchida, S. & Zaanen, J. From quantum matter to high-temperature superconductivity in copper oxides. *Nature* **518**, 179–186 (2015).
187. Joffre, O. P., Segura, E., Savina, A. & Amigorena, S. Cross-presentation by dendritic cells. *Nat. Rev. Immunol.* **12**, 557–569 (2012).
188. Kaminski, A. *et al.* Spontaneous breaking of time-reversal symmetry in the pseudogap state of a high-T_c superconductor. *Nature* **416**, 610–613 (2002).
189. Fauqué, B. *et al.* Magnetic Order in the Pseudogap Phase of High-T_c Superconductors. *Phys. Rev. Lett.* **96**, 197001 (2006).
190. Li, Y. *et al.* Hidden magnetic excitation in the pseudogap phase of a high-T_c superconductor. *Nature* **468**, 283–285 (2010).
191. Varma, C. Mind the pseudogap. *Nature* **468**, 184–185 (2010).
192. Grissonnanche, G. *et al.* Giant thermal Hall conductivity in the pseudogap phase of cuprate superconductors. *Nature* **571**, 376–380 (2019).
193. Grissonnanche, G. *et al.* Chiral phonons in the pseudogap phase of cuprates. *Nat. Phys.* **16**, 1108–1111 (2020).
194. Collignon, C. *et al.* Fermi-surface transformation across the pseudogap critical point of the cuprate superconductor $La_{1.6-x}Nd_{0.4}Sr_xCuO_4$. *Phys. Rev. B* **95**, 224517 (2017).
195. Michon, B. *et al.* Thermodynamic signatures of quantum criticality in cuprate superconductors. *Nature* **567**, 218–222 (2019).
196. Cyr-Choinière, O. *et al.* Pseudogap T^* of cuprate superconductors from the Nernst effect. *Phys.*

Rev. B **97**, 064502 (2018).
197. Prasai, N. *et al.* Spin phases of the helimagnetic insulator Cu_2OSeO_3 probed by magnon heat conduction. *Phys. Rev. B* **99**, 020403 (2019).
198. Chacon, A. *et al.* Observation of two independent skyrmion phases in a chiral magnetic material. *Nat. Phys.* **14**, 936–941 (2018).
199. Qian, F. *et al.* New magnetic phase of the chiral skyrmion material Cu_2OSeO_3. *Sci. Adv.* **4**, (2018).
200. Lee, S. & Li, X. Hydrodynamic phonon transport: past, present and prospects. in 1-1-1–26 (IOP Publishing, 2020).
201. Peierls, R. Zur kinetischen Theorie der Wärmeleitung in Kristallen. *Ann. Phys.* **395**, 1055–1101 (1929).
202. Shi, L. Nonresistive heat transport by collective phonon flow. *Science.* **364**, 332–333 (2019).
203. Martelli, V., Jiménez, J. L., Continentino, M., Baggio-Saitovitch, E. & Behnia, K. Thermal Transport and Phonon Hydrodynamics in Strontium Titanate. *Phys. Rev. Lett.* **120**, 125901 (2018).
204. Alexander, M. G., Goshorn, D. P. & Onn, D. G. Low-temperature specific heat of the graphite intercalation compounds KC_8, CsC_8, RbC_8, and their parent highly oriented pyrolytic graphite. *Phys. Rev. B* **22**, 4535–4542 (1980).
205. Komatsu, K. Theory of the Specific Heat of Graphite II. *J. Phys. Soc. Japan* **10**, 346–356 (1955).
206. Huberman, S. *et al.* Observation of second sound in graphite at temperatures above 100 K. *Science.* **364**, 375–379 (2019).
207. Ding, Z. *et al.* Observation of second sound in graphite over 200 K. *Nat. Commun.* **13**, 285 (2022).
208. Gooth, J. *et al.* Thermal and electrical signatures of a hydrodynamic electron fluid in tungsten diphosphide. *Nat. Commun.* **9**, 4093 (2018).
209. Guyer, R. A. & Krumhansl, J. A. Thermal Conductivity, Second Sound, and Phonon Hydrodynamic Phenomena in Nonmetallic Crystals. *Phys. Rev.* **148**, 778–788 (1966).
210. Akhiezer, A. I., Bar'yakhtar, V. G. & Kaganov, M. I. Spin Waves in Ferromagnets and Antiferromagnets. II Interaction of Spin Waves with One Another and with Lattice Vibrations; Relaxation and Kinetic Processes. *Sov. Phys. Uspekhi* **3**, 661–676 (1961).
211. Forney, J.-J. & Jäckle, J. Second sound and heat conduction of magnons in the ferromagnetic Eu-chalcogenides. *Phys. der Kondens. Mater.* **16**, 147–162 (1973).
212. Cui, L. *et al.* Quantized thermal transport in single-atom junctions. *Science.* **355**, 1192–1195 (2017).
213. Cui, L. *et al.* Thermal conductance of single-molecule junctions. *Nature* **572**, 628–633 (2019).
214. Kim, J., Ou, E., Sellan, D. P. & Shi, L. A four-probe thermal transport measurement method for nanostructures. *Rev. Sci. Instrum.* **86**, 044901 (2015).
215. Olsson, K. S. *et al.* Temperature-dependent Brillouin light scattering spectra of magnons in yttrium iron garnet and permalloy. *Phys. Rev. B* **96**, 024448 (2017).
216. An, K. *et al.* Magnons and Phonons Optically Driven out of Local Equilibrium in a Magnetic Insulator. *Phys. Rev. Lett.* **117**, 107202 (2016).
217. Olsson, K. S. *et al.* Temperature dependence of Brillouin light scattering spectra of acoustic phonons in silicon. *Appl. Phys. Lett.* **106**, 051906 (2015).

218. Sullivan, S. *et al.* Optical Generation and Detection of Local Nonequilibrium Phonons in Suspended Graphene. *Nano Lett.* **17**, 2049–2056 (2017).
219. Kargar, F. & Balandin, A. A. Advances in Brillouin–Mandelstam light-scattering spectroscopy. *Nat. Photonics* **15**, 720–731 (2021).
220. Sothmann, B. & Hankiewicz, E. M. Fingerprint of topological Andreev bound states in phase-dependent heat transport. *Phys. Rev. B* **94**, 081407 (2016).
221. Fornieri, A. & Giazotto, F. Towards phase-coherent caloritronics in superconducting circuits. *Nat. Nanotechnol.* **12**, 944–952 (2017).
222. Li, C. *et al.* Commensurate lattice constant dependent thermal conductivity of misoriented bilayer graphene. *Carbon N. Y.* **138**, 451–457 (2018).
223. Ren, W. *et al.* The Impact of Interlayer Rotation on Thermal Transport Across Graphene/Hexagonal Boron Nitride van der Waals Heterostructure. *Nano Lett.* **21**, 2634–2641 (2021).
224. Kim, S. E. *et al.* Extremely anisotropic van der Waals thermal conductors. *Nature* **597**, 660–665 (2021).
225. Cao, Y. *et al.* Unconventional superconductivity in magic-angle graphene superlattices. *Nature* **556**, 43–50 (2018).
226. Nasu, J., Yoshitake, J. & Motome, Y. Thermal Transport in the Kitaev Model. *Phys. Rev. Lett.* **119**, 127204 (2017).
227. Zhang, X., Zhang, Y., Okamoto, S. & Xiao, D. Thermal Hall Effect Induced by Magnon-Phonon Interactions. *Phys. Rev. Lett.* **123**, 167202 (2019).
228. Thingstad, E., Kamra, A., Brataas, A. & Sudbø, A. Chiral Phonon Transport Induced by Topological Magnons. *Phys. Rev. Lett.* **122**, 107201 (2019).